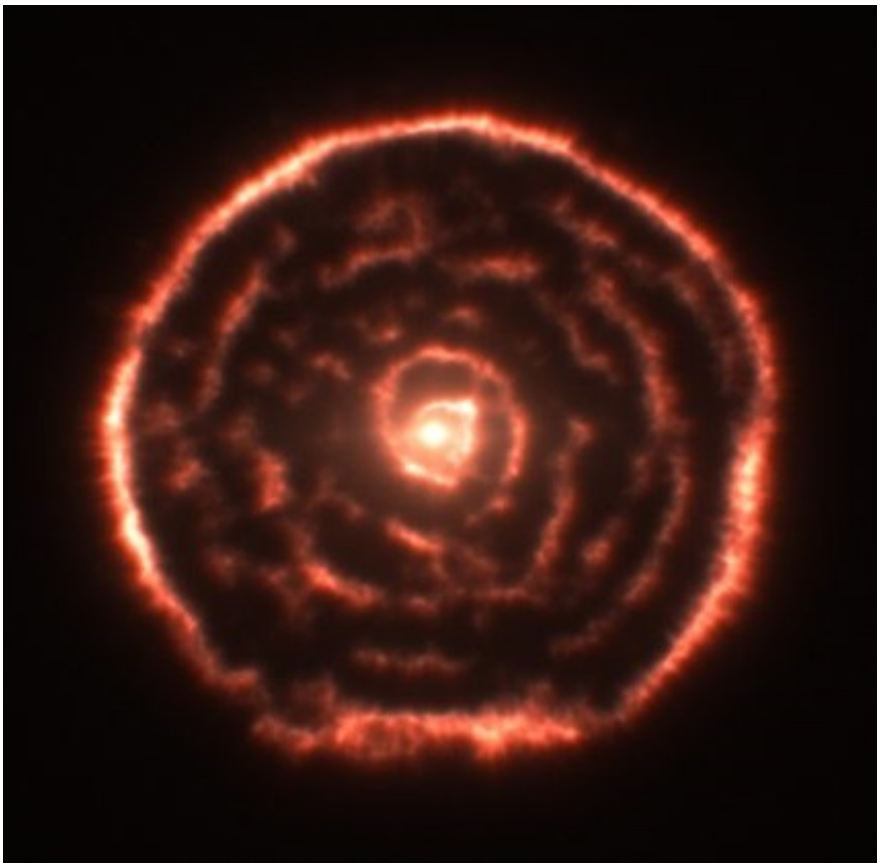

Chemical Diversity among Asymptotic Giant Branch Stars

Master's thesis in Physics

JOHANNA BRINKMALM

DEPARTMENT OF PHYSICS

CHALMERS UNIVERSITY OF TECHNOLOGY
Gothenburg, Sweden 2024
www.chalmers.se

Master's thesis 2024

Chemical Diversity among Asymptotic Giant Branch Stars

JOHANNA BRINKMALM

CHALMERS
UNIVERSITY OF TECHNOLOGY

Department of Physics
Department of Space, Earth and Environment
Chalmers University of Technology
Gothenburg, Sweden 2024

Chemical Diversity among Asymptotic Giant Branch Stars
JOHANNA BRINKMALM

Supervisor: Elvire De Beck, Department of Space, Earth and Environment
Examiner: Elvire De Beck, Department of Space, Earth and Environment

Master's Thesis 2024
Department of Space, Earth and Environment
Chalmers University of Technology
SE-412 96 Gothenburg
Telephone +46 31 772 1000

Cover: ALMA Observations image of an unexpected spiral structure in the material around the old star R Sculptoris. Credit: ALMA (ESO/NAOJ/NRAO)/M. Maercker et al.

Typeset in LaTeX
Printed by Chalmers Reproservice
Gothenburg, Sweden 2024

Chemical Diversity among Asymptotic Giant Branch Stars
JOHANNA BRINKMALM
Department of Physics
Chalmers University of Technology

Abstract

Stars with masses between roughly 0.8 and 8 $M_{\odot}$ will evolve into asymptotic giant branch (AGB) stars at the end of their lives. AGB stars are characterised by high luminosities and low surface temperatures. During the AGB phase, strong mass loss by outflows takes place and results in the formation of the large, cool and diluted circumstellar envelope (CSE) around the star. AGB stars are highly obscured due to the CSE containing a high amount of dust. Therefore, the chemical and physical properties of AGB stars must be studied through the CSE, which can be investigated by studying molecular-line observations. The DEATHSTAR project has studied the CO $J = 2 \rightarrow 1$ and $3 \rightarrow 2$ emission lines for a large sample of nearby, southern AGB stars. In this project, ∼70 of these sources were considered (25 M-type, 15 S-type, and 27 C-type stars). The DEATHSTAR study also included observations of other molecules such as ^{13}CO, SiO, CS, SiS and SO_2, which are the main focus of this project. The sources were observed with the Atacama Large Millimeter Array (ALMA). The data was provided in the form of data cubes from which spectra could be extracted. In these spectra, molecular lines were identified using the Splatalogue database for astronomical spectroscopy. The integrated intensities of these lines could then be used as a proxy for the molecular abundance. The trend found for most species was that the intensity measure, I_{scaled}, either did not vary much with stellar envelope density or decreased with increasing stellar envelope density. However, this decrease was not to the same degree as for the molecular abundance seen in other studies. In the case of decreasing intensity measure with envelope density, the trend could be interpreted as supporting evidence of the species in question being incorporated onto dust grains. However, abundance estimates based on radiative transfer modeling are necessary to reliably draw such conclusions.

Keywords: AGB stars, circumstellar envelope, chemical diversity in AGB stars, molecular abundance proxy.

Acknowledgements

First of all I would like to thank my supervisor Elvire De Beck. Throughout the year she has guided and encouraged me, and patiently helped me with all sorts of problems. I would also like to thank Kelly Ma and Theo Khouri for generously providing me with some of the tools that I used in this project. I am also very grateful for the advice and knowledge shared by Matthias Maercker, Miora Andriantsaralaza, Ramlal Unnikrishnan Nair and Johan Gustafsson. Finally, I'm very thankful to my friends and family for their constant love and support.

Johanna Brinkmalm, Gothenburg, January 2024

Contents

1

Introduction

The evolution a star goes through is dominated by the star's mass at its birth. Low- and intermediate-mass stars ($\sim 0.8\ M_\odot < M < 8\ M_\odot$) will, near the end of their lives, evolve into asymptotic giant branch (AGB) stars [1]. AGB stars are very bright and can reach luminosities up to several $10^4\ L_\odot$. However, their surfaces are also very cool, with effective temperatures of $\sim$ 2000 K to 3000 K, which implies that they have very large radii (several hundred $R_\odot$) [2]. This corresponds to sizes larger than the Earth's orbit around the Sun. AGB stars consist of a small and very hot degenerate C-O core, a large and hot envelope, a warm atmosphere that is very thin compared to the rest of the star, and a cool circumstellar envelope (CSE) that is very large and diluted. The AGB phase is characterized by strong mass loss by outflows from the star, and it is these outflows that result in the CSE around the star.

1.1 Stellar evolution up to the AGB phase

Before the star reaches the AGB phase it goes through several evolutionary stages. In Figure 1.1 a Hertzsprung–Russell-diagram (HR-diagram), showing stellar luminosity versus surface temperature, is found. Here, most stars are located on the so-called main sequence (MS) which is the longest of the evolutionary stages. However, in the upper right corner, some stars have cooler surface temperatures along with higher luminosities. These so-called giants and supergiants are stars that are nearing the end of their lifetimes. This is also where the AGB stars are located in the HR-diagram.

During the main sequence, the energy production is due to active nuclear processes that take place in the hot stellar core [2]. Here, hydrogen (H) is converted into helium (He), but also into carbon (C), nitrogen (N) and oxygen (O). There are two nuclear reactions that convert hydrogen into these heavier elements, and which is dominating depends on the mass of the star. For lower mass stars ($\mathrm{M} < 1.3\ M_\odot$) the energy production is dominated by hydrogen fusion through the proton-proton chain, while in higher mass stars ($M > 1.3\ M_\odot$) the CNO cycle dominates instead.

The main sequence is over when H in the core is exhausted, leaving the star with a core consisting of He. The energy production is halted and with it also the ra-

diation pressure that counteracts the self-gravitation of the star. This results in a contraction of the He-core, which in turn leads to a shell above the core reaching high enough temperatures to start shell-H burning. This conversion of H into He in this shell is now the source of nuclear-energy production [2].

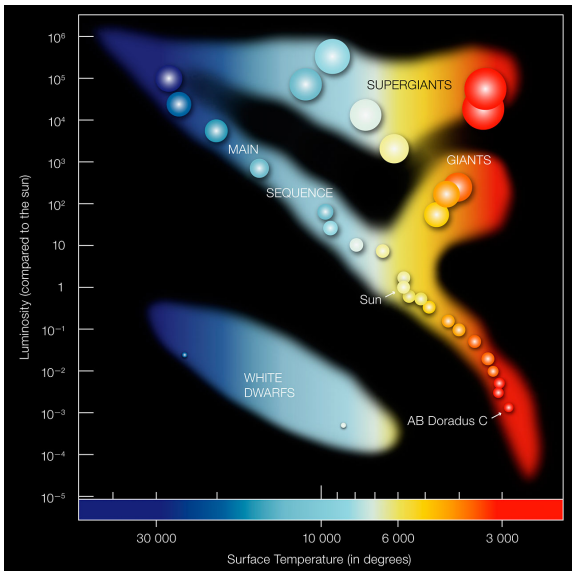

Figure 1.1: A Hertzsprung–Russell-diagram (HR-diagram) [3], showing stellar luminosity versus surface temperature.

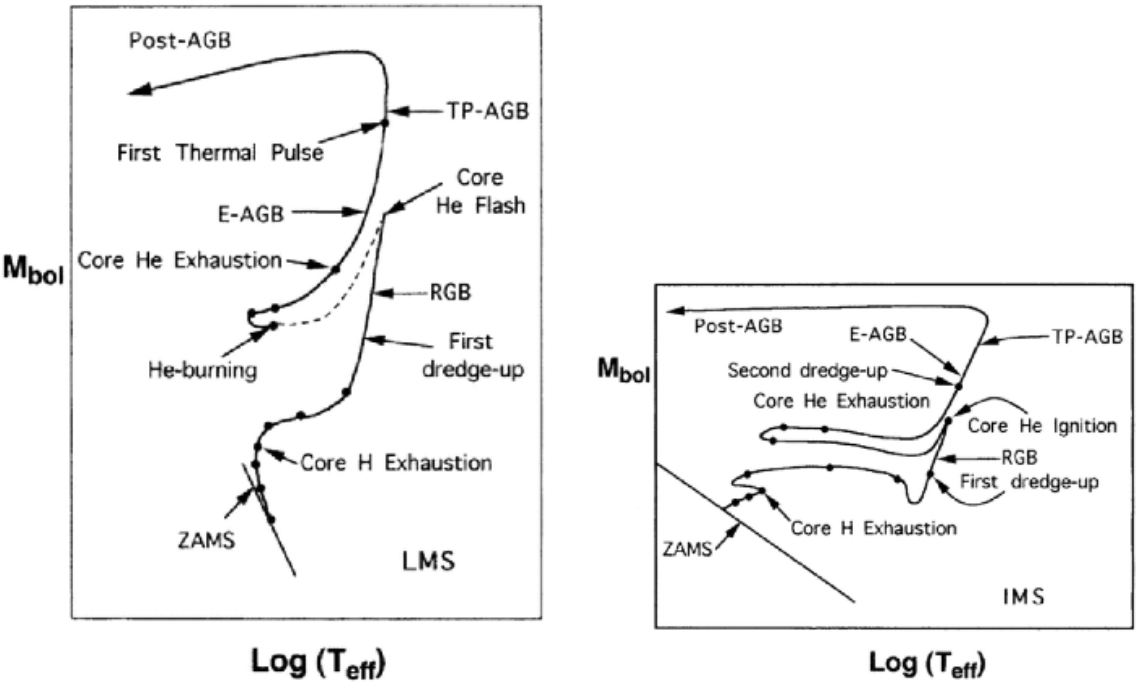

(a) Evolutionary path of a 1 $M_\odot$ star. **(b)** Evolutionary path of a 5 $M_\odot$ star.

Figure 1.2: Illustration of the evolutionary paths of two stars with different masses [4].

In Figure 1.2 the evolutionary paths of two different stars in the HR-diagram can be found. As the He-core contracts, the star is rapidly evolving horizontally to the right in the HR diagram. This is due to the outer layers of the star expanding which leads to a drastic decrease in surface temperature. The temperature decrease in the outer parts will result in the formation of a convective envelope, which leads to increasing efficiency of energy transport and in turn an increase in luminosity. The star now appears as a red giant with $L \sim$ a few 100 $L_\odot$ and low surface temperatures of around 2000-4000 K [2]. During this phase the convective envelope will reach down to the inner layers and bring up material formed in the nuclear processes that take place there up to the stellar surface. This so-called first dredge-up (FDU) changes the surface composition of the star. The star continues to move up the red giant branch (RGB).

In the case of stars with $M < 2\ M_\odot$, the He-core will, during contraction on the RGB, become degenerate. The core's temperature will no longer increase, but its mass, however, will continue to increase as the star moves further up the RGB. Eventually, when $M_{\text{core}} \sim 0.45\ M_\odot$ [2], the star will go through a so-called He-flash where the core degeneracy is lifted. This occurs at the tip of the RGB (see Figure 1.2a). For stars with $M > 2\ M_\odot$ there will be no He-flash (see Figure 1.2b).

The core temperature continues to increase and helium fusion is initiated gradually when the temperature is high enough ($\sim 10^8$ K). This nuclear process, called the 3α-process, transforms three He atoms into one C atom [2]. The core will expand again due to the pressure increasing, which leads to the contraction of the envelope and a decrease in luminosity. The star's evolution on the RGB is now over and it proceeds to the He-main sequence.

Eventually, the He in the core will be exhausted as well and the stellar core will then consist of carbon and oxygen. Thus, the star will have a C-O core as well as an inner and an outer shell where He and H are burning, respectively. Higher mass stars will continue to go through stages of burning heavier and heavier elements in the core, but lower and intermediate mass stars will never reach a high enough core temperature for that to happen. Instead, similarly to when hydrogen was exhausted in the core, the core will contract leading to the expansion of the outer layers. The star is now in its AGB phase.

1.2 The AGB phase

As mentioned above, AGB stars consist of a small and very hot core, a large and hot envelope, a thin, warm atmosphere, and a cool, large circumstellar envelope (CSE).

At this stage the stellar core consists mainly of C, O, and degenerate electrons [2]. In the earlier stages, the stellar evolution was dominated by the core's evolution. This is no longer the case.

The stellar envelope contains two nuclear burning shells that are separated by an intershell region [2]: the He-burning shell, that is closest to the core, and the H-

burning shell, located outside the He-burning shell. Outside of these, there is a large convective envelope that reaches up to the surface of the star. Stars more massive than 4 $M_\odot$ go through a second dredge-up (SDU). Similarly to the FDU, the large convective envelope reaches down to the nuclear burning layers and brings up material from the H-shell region to the stellar surface. Thus, the AGB star surface will contain material produced in the CNO-cycle.

In the early AGB phase, He-shell burning dominates the energy production at first, but after a time of only He-shell burning, the star will enter into a double-shell burning phase, where H-shell burning takes place outside the He-shell burning [2]. Due to the H-shell burning, He will accumulate until the energy production through the shell-He burning will start again in a thermonuclear runaway process, called the He shell flash. This will lead to convectional instabilities as the H-shell is pushed out into cooler areas of the star and consequently shut off. Thus, the convective envelope can reach down through this region to the intershell zone, from which 3α-process products can be transported upwards to the stellar surface. In this so-called third dredge up (TDU), mainly He and ^{12}C will be mixed upwards and thus change the surface composition. However, in order to significantly change the surface abundances, several TDU events are needed. This process as a whole is called a thermal pulse (TP) and it lasts for a few hundred years. The intensity and the number of TPs depend on the initial mass and chemical composition of the star. The time between two TPs is around $10^3 - 10^5$ years. In the case of stars with $M > 4\ M_\odot$, the base of the outer convective envelope can reach high enough temperatures for the CNO cycle to be initiated during this interpulse phase. This is known as hot bottom burning (HBB). The transport of CNO cycle products to the surface by the convective envelope will decrease the ^{12}C abundance and increase the ^{13}C and ^{14}N abundances at the stellar surface.

The AGB stars are classified into three chemical types depending on the C/O abundance ratio in the stellar atmosphere. Stars that are oxygen rich, with C/O < 1, are referred to as M-type stars, while carbon-rich stars (C/O > 1) are referred to as C-type stars [2]. Additionally, stars with C/O $\lesssim 1$ are known as S-type stars. This ratio will change during the AGB evolution of the star, depending on the star's mass and metallicity. TDUs will increase the C/O ratio as it brings ^{12}C to the surface, while HBB will lower the ratio since it reprocesses ^{12}C in the CNO cycle. Thus, the surface chemistry of an AGB star can tell us about the internal processes as well as the evolutionary state of the star.

The slow neutron-capture process (s-process) is typical in AGB stars and occurs in the intershell region between the He- and the H-burning shells [2]. This process is characterized by a slow neutron capture that is then followed by β-decay. During the TDU, products of the s-process are transported to the stellar surface. These products are commonly found in S-type stars.

During the AGB phase the stars have radii of several 100 $R_\odot$. Because the stellar masses are $< 8M_\odot$, the resulting surface gravity is well below that of a sun-like star [5]. The AGB stars are therefore prone to lose mass from the atmosphere, since it

is so loosely bound to the surface, if a process takes place that can accelerate the atmospheric gas beyond the escape velocity. Such a phenomenon is the dynamical levitation of the atmosphere due to shock waves that are triggered by stellar pulsation. The partial ionization of H and He in the thin stellar atmosphere are what leads to the outer convective envelope layers pulsating [2]. These pulsations create sound waves that travel outwards through the outer parts of the star. As the density and temperature decrease drastically in the stellar atmosphere, these waves become supersonic shock waves that heat and compress the material in front of it. This leads to AGB stars experiencing mass loss in the form of slow and massive winds. During the AGB phase it is the mass loss rather than the nuclear processes that determines the star's evolution, as changes in the rate at which the star loses mass can affect the evolution and the nucleosynthesis of the star. This material that is ejected outwards forms the expanding, chemically rich, envelope around the star - the circumstellar envelope (CSE).

The CSE contains the products of the elements produced by nuclear processes in the star's inner layers and brought up to the surface during the TDU, as well as dust grains formed near the photosphere [6]. In this way, AGB stars and their outflows contribute to the chemical evolution of the interstellar medium.

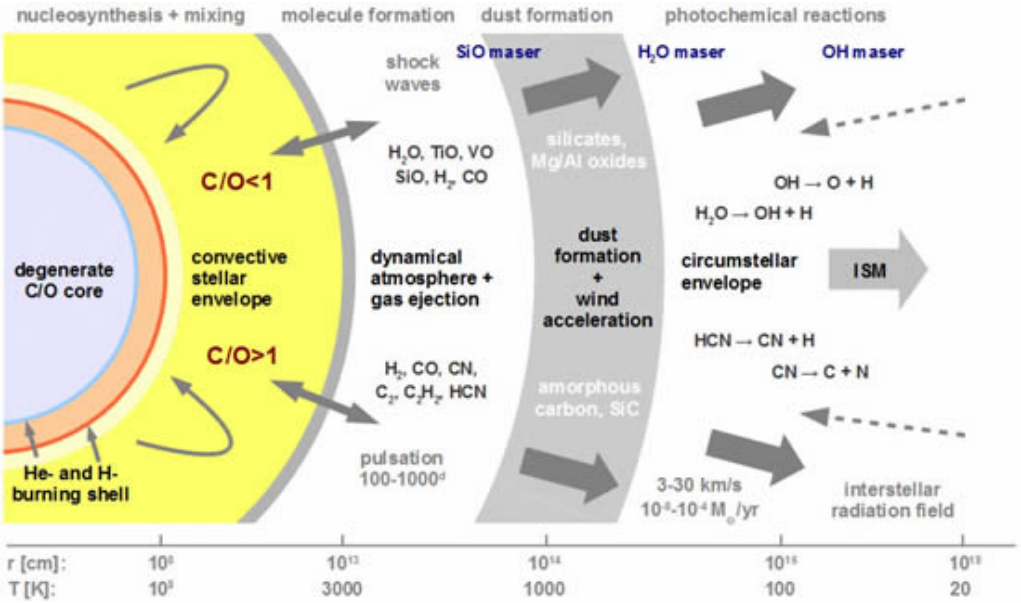

Figure 1.3: A schematic representation of the chemical structure of the CSE of an AGB star. The upper half represents M-type stars, whereas the lower part represents C-type stars. At the very bottom, a scale indicating distance and temperature is found. An indication of the different zones can be found at the very top. [7]

The classification of C-, M- and S-type stars mentioned above is not only useful when studying the chemical properties of the stellar surface, but also when studying the chemistry in the CSE. The molecular bond of CO is very strong, therefore most carbon and oxygen will be locked into CO when C/O$<$ 1 and C/O$>$ 1 respectively [2]. This means that, in the CSEs of M-type stars, one expects to see a high

abundance of oxygen-bearing molecules (other than CO). Similarly in the CSEs of C-type stars, one expect to see a high abundance of carbon-bearing molecules.

AGB stars are highly obscured due to the large amount of dust in the CSEs around them [6]. Therefore, an estimate of the photospheric abundances of these stars often must be based on circumstellar emission. Hence, in order to understand the chemical and physical properties of AGB stars, it is important to gain more knowledge about their circumstellar molecular line emission.

1.3 Molecular lines

The properties of the CSEs, both physical and chemical, can be investigated by studying molecular-line observations. A molecule is characterized by its discrete energy levels, which are a measure of its electronic, vibrational and rotational states [2]. A range of vibrational states can be found within every electronic state. The vibration of these molecules includes every type of oscillatory motion of the molecule's nuclei, such as bending and stretching of the molecular bonds. A molecule also has rotational states that are due to the irradiating electromagnetic field exerting a torque on the molecular dipole. The transitions between these rotational molecular states are observed at longer wavelengths, such as the far-infrared (FIR), (sub)millimeter, and centimeter range. Additionally, some molecules have fine structure, which is a further division of their energy spectrum due to spin-orbit coupling.

Some of the detected rotational transitions are maser (Microwave Amplification by Stimulated Emission of Radiation) lines, which can be brighter than other molecular lines. A maser is a naturally occurring source of stimulated spectral line emission [8]. Emission from a maser is stimulated and coherent, similarly to a laser. However, this only occurs if there is a population inversion, which is a non-thermal process where there are more molecules with electrons in the higher energy state than the lower state. An external energy source is needed for this scenario, a so-called pumping mechanism. This will lead to a chain-reaction, which in turn leads to a photon being exponentially amplified by the gain medium. The frequency of the emission will correspond to the difference in energy between the two energy levels of the species in the gain medium.

1.4 The DEATHSTAR project

The data used in this project was collected for the DEATHSTAR project, were the CO $J = 2 \rightarrow 1$ and $3 \rightarrow 2$ emission was observed for a large sample of nearby, southern AGB stars.

The main goal of the DEATHSTAR project is to use these observations in order to accurately measure the CO envelope sizes of the stars, which is a major source of uncertainty in current mass-loss rate estimates from AGB stars. Another goal is to investigate how common large-scale asymmetries in the envelopes are. This can be used to obtain a more accurate measure of the wind parameters of stellar outflows.

Additionally, the project hopes to determine gas-to-dust ratios of the stars in the sample. The study also includes observations of other molecules such as ^{13}CO, SiO, CS, SiS and SO_2.

The DEATHSTAR sample consists of $\sim$ 200 AGB stars. However, the project presented in this report only considered $\sim$ 70 southern sources, with declinations lower than $+15^o$. This sample consists of 25 M-type, 15 S-type, and 27 C-type stars. These sources were observed with the Atacama Large Millimeter Array (ALMA), located in the Atacama desert in Chile. The observations were done during ALMA Cycle 4 and 5 with the 7 m Atacama Compact Array (ACA) in stand-alone mode in bands 6 and 7 with four spectral windows in each band. In Band 6 the spectral windows were centered on 216.4, 218.3, 230.7, and 232.1 GHz, while in band 7 they were centered on 330.75, 332.25, 343.52, and 345.6 GHz [9]. In addition to this, the four sources AI Vol, AFGL 3068, R Dor, and IRC-30398, the stars with the largest angular scales, were observed with the 12 m total power (TP) antennas in Cycle 5 as well in order to recover flux that was not captured by the ACA observations.

1.5 Aims

The aim of this thesis project is to study the chemical diversity in a large sample of AGB stars from the DEATHSTAR project and, for a selection of molecules, compare a first-order estimate of the abundance of a given molecule in different chemical types of AGB stars. This study will hopefully produce results that future studies can follow up on.

1.6 Limitations

The overall goal of the DEATHSTAR project is to lower the uncertainties of the observational estimates of mass-loss rates from AGB stars. Since CO as well as the CO envelope sizes already have been analyzed in more detail, this project will not investigate this any further. For the same reason, this project will also not investigate the mass-loss rates of these stars. The lines of the additional molecules are the ones that will be focused on in this project. Finally, this project will not estimate the molecular abundance using radiative transfer modeling. Instead a first order proxy for the abundance will be used.

Source	$\dot{M}$ [$M_\odot$/yr]	D [pc]	v_{LSR} [km/s]	v_{exp} [km/s]
BK Vir	1.5×10^{-7}	190	17.0	11.0
CW Cnc	5×10^{-6}	280	15.0	23.3
IRC+10365	3×10^{-5}	750	-31.3	35.5
IRC-10529	2.5×10^{-6}	270	-17.5	30.0
IRC-30398	1.1×10^{-5}	600	-6.5	36.6
L_2 Pup	2×10^{-8}	85	32.7	8.0
R Crt	8×10^{-7}	170	11.3	23.5
R Dor	1.3×10^{-7}	45	7.0	14.7
R Hor	5.9×10^{-7}	310	37.5	13.0
R Hya	3×10^{-7}	150	-9.8	21.5
R Leo	2×10^{-7}	130	-0.5	16.0
RR Aql	2.4×10^{-6}	530	27.8	16.5
RT Vir	5×10^{-7}	170	17.3	17.5
SU Vel	2×10^{-7}	250	7.5	13.0
SV Aqr	3×10^{-7}	470	6.8	18.5
SW Vir	4×10^{-7}	120	-11.5	17.0
T Mic	8×10^{-8}	130	25.0	13.0
θ Aps	4×10^{-8}	110	0.8	13.1
U Men	2×10^{-7}	320	15.6	25.3
UY Cet	2.5×10^{-7}	300	4.8	15.5
V 1943 Sgr	1.3×10^{-7}	150	-15.0	13.0
V Tel	2×10^{-7}	290	-32.8	15.5
W Hya	8×10^{-8}	65	41.0	17.5
WX Psc	1.1×10^{-5}	600	9.5	39.0
Y Scl	1.3×10^{-7}	330	29.0	12.0

Table 1.1: Table containing the mass-loss rate $\dot{M}$, distance D, systemic velocity v_{LSR} and expansion velocity v_{exp} for the M-type sources from the DEATHSTAR sample considered in this project. Table values are adopted from [1] and [9].

Source	$\dot{M}$ [$M_\odot$/yr]	D [pc]	v_{LSR} [km/s]	v_{exp} [km/s]
AFGL 3068	1×10^{-5}	980	-31.4	28.7
AI Vol	4.9×10^{-6}	710	-38.8	26.2
AQ Sgr	2.5×10^{-7}	420	21.5	23.0
CZ Hya	9×10^{-7}	960	13.3	25.5
NP Pup	6.5×10^{-8}	420	12.8	21.5
R For	1.1×10^{-6}	610	-2.3	33.5
R Lep	7×10^{-7}	250	11.5	38.0
RT Cap	1×10^{-7}	450	-18.0	15.0
RV Aqr	2×10^{-6}	670	1.3	30.5
R Vol	1.7×10^{-6}	730	-10.8	36.5
SS Vir	2×10^{-7}	540	8.7	30.3
T Ind	9×10^{-8}	570	15.8	11.5
TW Hor	9×10^{-8}	400	1.1	13.8
TW Oph	5×10^{-8}	280	28.5	17.0
U Hya	1.2×10^{-7}	160	-31.3	14.5
V Aql	1.5×10^{-7}	370	53.8	19.5
V 688 Mon	6.1×10^{-6}	1770	3.0	27.0
V 821 Her	3×10^{-6}	600	-0.2	27.1
V 996 Cen	1×10^{-7}	390	-1.9	25.6
V 1259 Ori	8.8×10^{-6}	1660	43.3	28.5
V 1302 Cen	1×10^{-7}	530	-42.8	17.8
W CMa	3×10^{-7}	450	-0.3	21.5
W Ori	1.4×10^{-7}	220	-1.5	23.0
X TrA	1.3×10^{-7}	360	-3.8	20.0
X Vel	1.8×10^{-7}	310	-19.3	22.5
Y Hya	1.9×10^{-7}	350	-8.5	18.0
Y Pav	1.6×10^{-7}	360	-3.5	18.0

Table 1.2: Same as Table 1.1 but for the C-type sources considered in this project. Table values are adopted from [1] and [9].

Source	$\dot{M}$ [$M_\odot$/yr]	D [pc]	v_{LSR} [km/s]	v_{exp} [km/s]
AM Cen	1.5×10^{-7}	750	-27.6	9.9
DY Gem	7×10^{-7}	680	-16.4	21.3
FU Mon	2.7×10^{-7}	780	-41.8	5.7
GI Lup	5.5×10^{-7}	690	5.3	23.7
IRC-10401	3.5×10^{-7}	430	20.5	37.1
NSV 24833	3×10^{-7}	610	58.3	21.5
RT Sco	4.5×10^{-7}	270	-46.2	28.9
RZ Sgr	3×10^{-6}	730	-25.0	16.3
ST Sco	1.5×10^{-7}	380	-4.3	13.8
ST Sgr	2×10^{-7}	540	57.0	17.3
T Sgr	1.4×10^{-7}	590	9.8	21.2
T Cet	4×10^{-8}	240	18.1	14.5
TT Cen	2.5×10^{-6}	880	6.4	42.3
UY Cen	1.3×10^{-7}	590	-24.4	29.2
Z Ant	9×10^{-8}	470	-15.5	16.5

Table 1.3: Same as Table 1.1 but for the S-type sources considered in this project. Table values are adopted from [1].

2

Method

2.1 Data extraction

There was no data collection in this project since the data has already been provided in the form of data cubes. A source is observed at several frequencies with ALMA and an image is obtained at every frequency. The result is a data cube with three dimensions: two spatial dimensions corresponding to the observed area on the sky plane and the third dimension being frequency. Furthermore, every pixel in the image has a corresponding spectrum of flux versus frequency. From these data cubes, spectra from four spectral windows in band 6 and in band 7 respectively could be extracted using the Common Astronomy Software Application package (CASA). As mentioned in Section 1.4, the spectral windows in band 6 were centered on 216.4, 218.3, 230.7, and 232.1 GHz, while the windows in band 7 were centered on 330.75, 332.25, 343.52, and 345.60 GHz.

2.2 Finding features in the spectra

For the extracted spectra, the rms noise level, σ, was defined from fitting a Gaussian function to the signal distribution (see Figure 2.1a) since the noise is expected to be Gaussian in nature. We use 3σ as a threshold for signal detection. More specifically, if two or more consecutive channels had flux values above 3σ, these were considered to be a potential spectral line. The minimum and maximum frequency corresponding to the first and last of these consecutive channels are designated f_{min} and f_{max} respectively.

The spectra all have a native frequency resolution, which is the difference in frequency between two adjacent channels. However, in order to recover additional scientifically valuable signal, the spectra can be smoothed and studied at a lower resolution. Smoothing by a factor of N results in a noise reduction by a factor $\sqrt{N}$. The maximum level of smoothing reasonable was deemed to correspond to six channels across a line, which in turn corresponds to a linewidth in velocity space of $2v_{exp}$. The new lowered resolution was then $\frac{2 \cdot v_{exp}}{6}$. Additionally, the spectra were smoothed to an intermediate resolution corresponding to twelve channels across a line, the resolution becoming $\frac{2 \cdot v_{exp}}{12}$. These three resolutions, the native as well as the two lowered resolutions, were used for finding features.

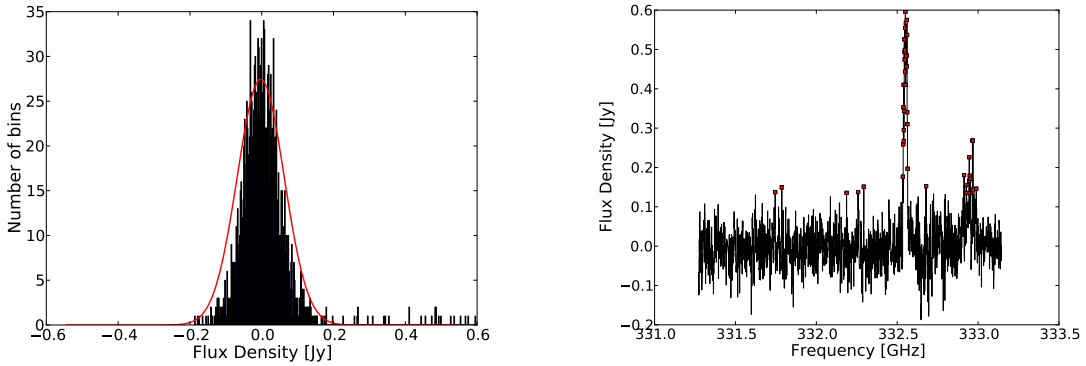

(a) **(b)**

Figure 2.1: (a) A Gaussian function being fitted to the signal distribution of a spectrum from AI Vol. (b) The corresponding spectrum, where the red rectangles indicate the channels with flux values above the 3σ threshold.

Figure 2.2: Spectrum of AI Vol for three different velocity resolutions. The dotted horizontal line represents the 3σ cutoff used to distinguish a signal from noise. The upper, middle and lower panels shows the native, $v_{res} = \frac{2 \cdot v_{exp}}{12}$ and the $v_{res} = \frac{2 \cdot v_{exp}}{6}$ resolution spectra respectively. The smoothing of the spectrum can make more lines, represented by the coloured vertical lines, distinguishable from noise.

Figure 2.2 shows an example of identifying features for the different resolutions. Here one can observe that smoothing the spectrum reduces noise and makes the signal clearer. However, smoothing to much can sometimes lead to the signal being flattened and to fewer identifications being made. For $v_{res} = \frac{2 \cdot v_{exp}}{12}$ smoothing leads to more spectral lines being identified compared to the native resolution. On the other hand, for $v_{res} = \frac{2 \cdot v_{exp}}{6}$ more identifications are being made compared to the native resolution, but fewer lines are identified compared to the intermediate resolution. This is an example of where smoothing a spectrum too much can lead to overlooking signals.

2.3 Identification of features

In order to identify features, molecular transitions within the interval $[f_{min} \cdot (1 - \frac{v_{exp}}{c}), f_{max} \cdot (1 + \frac{v_{exp}}{c})]$ were searched for using the Splatalogue database for molecular spectroscopy [10]. Here v_{exp} is the expansion velocity of the star and c is the speed of light. The extra term $\frac{v_{exp}}{c}$ accounts for the Doppler broadening of the spectral line due to v_{exp}. Splatalogue contains data on nearly six million spectral lines, such as transition frequency, quantum numbers and the energy level of the transition. Using Splatalogue to search within the frequency interval specified above, transitions located within that particular interval could be identified along with their characteristics. It is also possible to limit the search to certain isotopologues. The isotopologues listed in Table 2.1 were chosen because they have already been observed in similar stars and, therefore, are the ones most reasonable to be observed in this sample as well.

After identifying features using the Splatalogue catalogue, the identifications needed to be narrowed down in some cases. The reason for this is that all transitions for the specified isotopologues within the specified interval are being registered, regardless of how unlikely they are to correspond to the spectral line in question. This was done manually by comparing with other works or by studying tables, e.g [11], of the strengths of certain molecule transitions in order to see which was most likely to be visible. Figures 2.3 and 2.4 show an example of the rotational transitions identified in the spectra for the star AI Vol.

In Figure 2.5 a few examples of different line profiles are shown. Figure 2.5a is an example of a spectral feature that is rather representative of most features in terms of the line shape, which is Gaussian-like. The SiOv=1 line in Figure 2.5b is a maser line and thus much stronger. In this case it is also less symmetric than the SiOv=0 line in Figure 2.5a. Furthermore, some spectral lines are broader due to there being several transitions close together within that spectral line. This is due to the fine structure properties of that particular molecule. An example of this can be observed in 2.5c in the form of the AlO line. In cases such as this, a weighting of the strengths of the individual transitions in the line was done in order to get a single approximated frequency for the corresponding line. This frequency was then used for the conversion of the spectrum to velocity space for that particular line. There are also cases of more spread out fine structure, such as the case of ^{13}CN seen

Species	C-type	M-type	S-type
CO	Yes	Yes	Yes
^{13}CO	Yes	Yes	Yes
SiO	Yes	Yes	Yes
^{29}SiO	Yes	Yes	Yes
^{30}SiO	Yes*	Yes*	Yes*
SiS	Yes	Yes	Yes
^{29}SiS	Yes	Yes	Yes*
^{30}SiS	Yes	Yes	Yes*
Si^{33}S	Yes	Yes	Yes*
Si^{34}S	Yes*	Yes*	Yes*
CS	Yes	Yes	Yes
^{13}CS	Yes	Yes	Yes*
C^{34}S	Yes*	No	Yes*
^{13}CN	Yes	No	Yes*
CCH	Yes*	No	Yes*
CCCN	Yes*	No	Yes*
C_4H	Yes	No	Yes*
HCN	Yes*	No	Yes*
HNC	Yes*	No	Yes*
HC_3N	Yes	No	Yes*
HC_5N	Yes*	No	Yes*
HC^{15}N	Yes	No	Yes*
H^{13}CN	Yes	Yes	Yes
c-C_3H	Yes	No	Yes*
l-C_3H	Yes	No	Yes*
c-HCCCH	Yes	No	Yes*
SiN	Yes	No	Yes*
SiC_2	Yes	No	Yes*
Si^{13}CC	Yes	No	Yes*
AlF	Yes	No	Yes*
NaCl	Yes*	Yes*	Yes*
Na^{37}Cl	Yes	Yes	Yes*
SO	No	Yes	Yes
^{33}SO	No	Yes	Yes*
^{34}SO	No	Yes	Yes*
SO_2	No	Yes	Yes
$^{33}SO_2$	No	Yes*	Yes*
$^{34}SO_2$	No	Yes	Yes*
H_2O	No	Yes	Yes*
H_2S	No	Yes	Yes*
H_2CO	No	Yes	Yes*
AlO	No	Yes	Yes*
TiO_2	No	Yes*	Yes*

Table 2.1: Table of all isotopologues for which rotational transitions were searched for in Splatalogue as well as in which chemical type of star this was done. A certain isotopologue not being found in that chemical type of star is indicated by *.

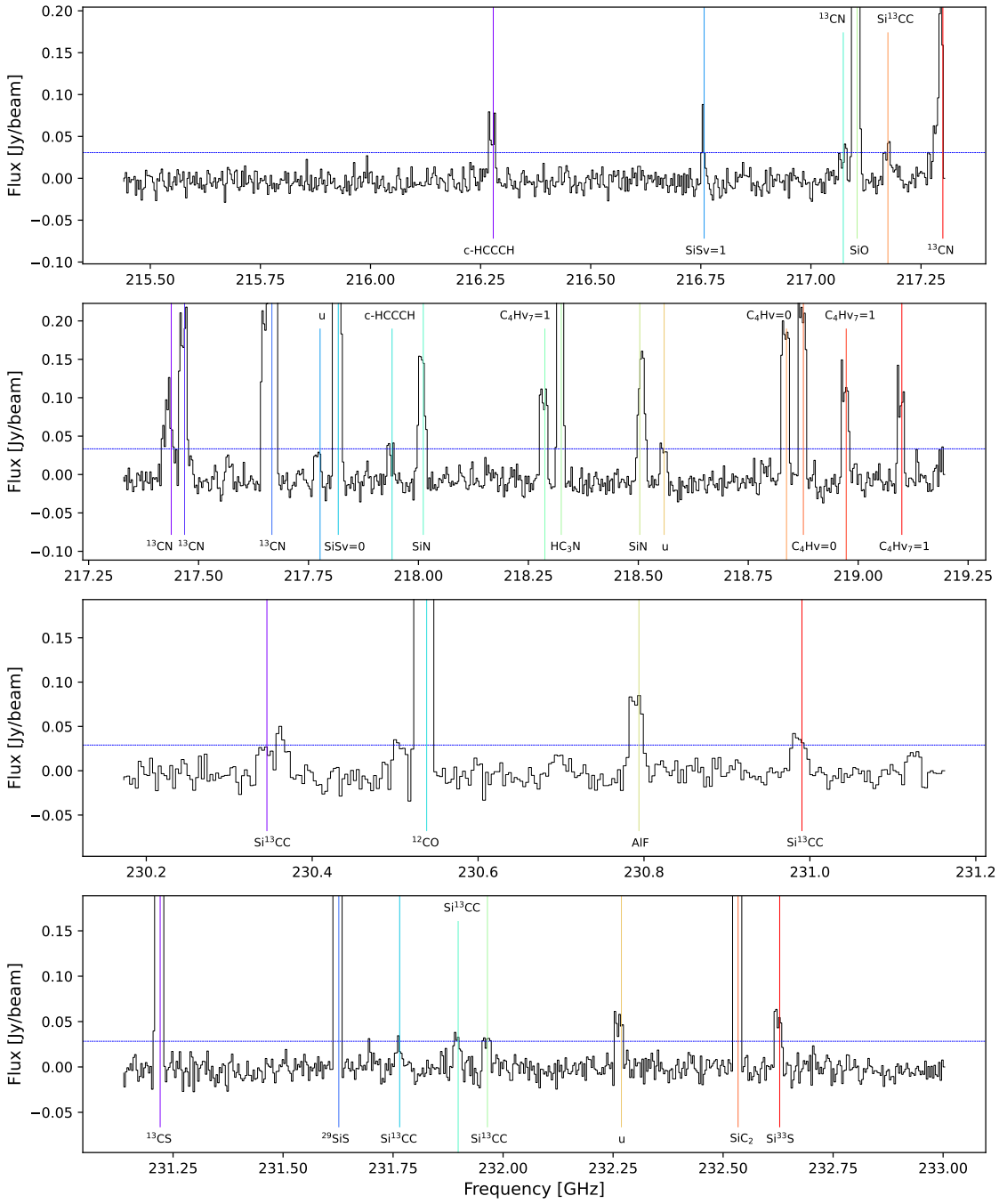

Figure 2.3: Four spectral windows for AI Vol in band 6. The dotted horizontal line represents the 3σ cutoff used to distinguish a signal from noise. The vertical lines represent the different transition frequencies for the lines, and are labeled with the corresponding isotopologue. Some transitions are only labeled u to indicate that it is an unidentified transition.

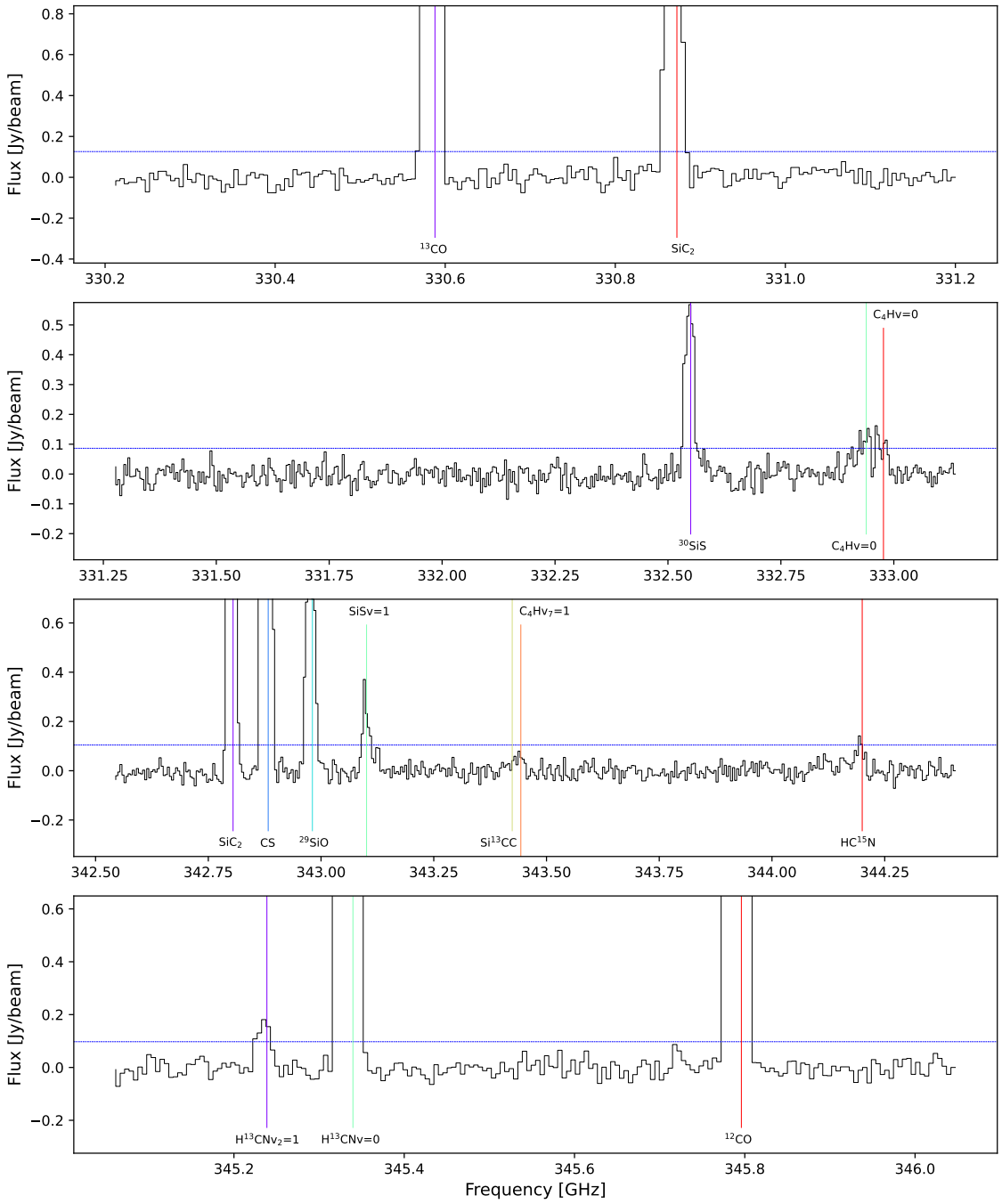

Figure 2.4: Same as Figure 2.3 but for four spectral windows in band 7.

in Figure 2.5d.

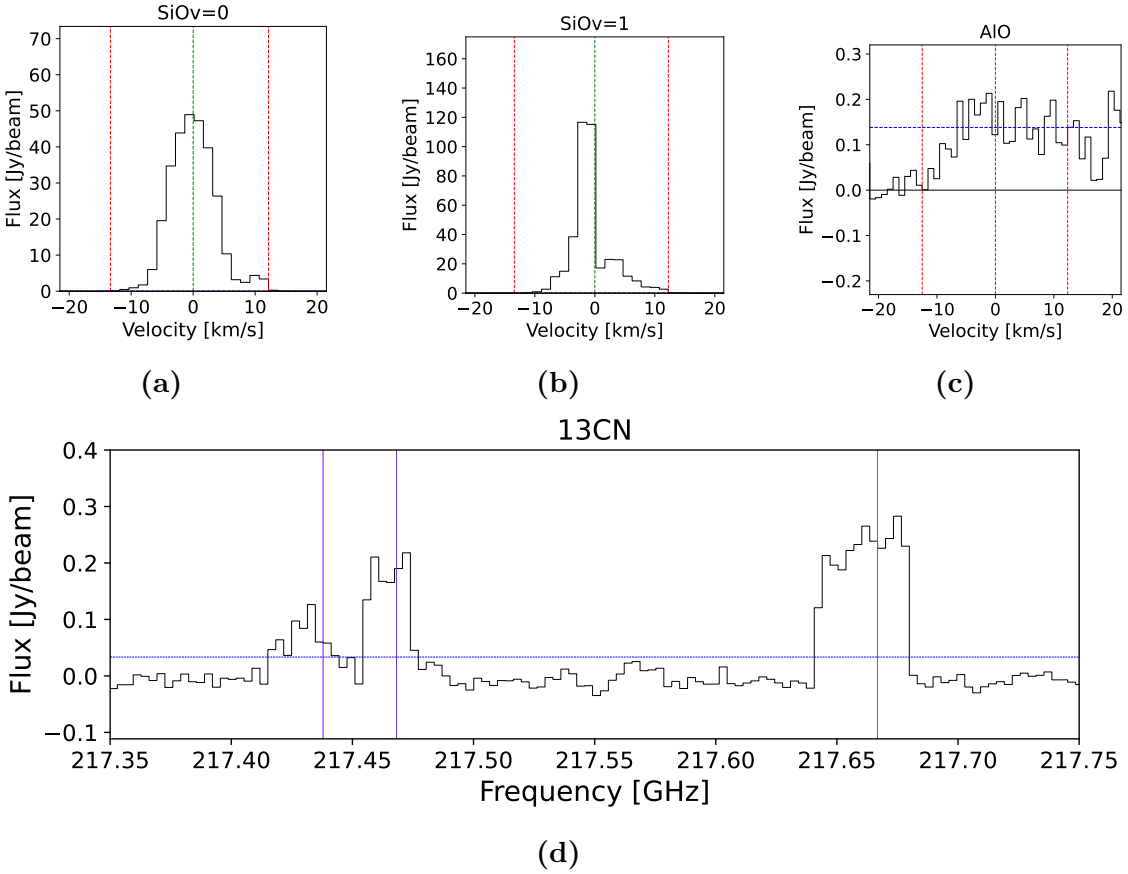

Figure 2.5: Four examples of spectral line profiles. The top 3 figures show spectral lines towards the M-type star W Hya. (a) Thermal emission from SiOv=0 J=5-4, (b) maser emission from SiOv=1 J=5-4, (c) broadened emission owing to hyperfine structure in AlO N=9-8,J=19/2-17/2,F=11-11. The green vertical corresponds to the transition frequency and the two red lines on either side correspond to $\pm v_{exp}$. The signal from AlO is significantly weaker than the SiO lines from the same star and therefore the 3σ level (horizontal blue line) is clearly seen. The bottom figure shows ^{13}CN emission towards the C-type star AI Vol, spread accross a large part of the spectrum owing to fine structure. The horizontal line corresponds to the 3σ level and the vertical lines correspond to the different transition frequencies of ^{13}CN.

2.4 Intensity measure I_{scaled}

Although radiation transfer effects prevent the measured line intensities from being a direct measure of molecular abundance, we can use them as zeroth-order proxies. Therefore, integrated intensities were calculated for each spectral line. The error in the calculated integrated intensity was assumed to be $\sim 20\%$ [9].

In order to compare the integrated intensities of the molecular transitions for the different sources, the distance has to be taken into account, as flux is inversely proportional to D^2, where D is the distance to the source. Furthermore, as the line intensity is affected by the number of emitting molecules, which depends on both the total mass available and molecular abundance, we also scale with mass-loss rate. Thus, the integrated intensity was scaled accordingly:

$$I_{\text{scaled}} = \frac{I \cdot (D/1kpc)^2}{\dot{M}}, \tag{2.1}$$

where I is the integrated intensity of the spectral line, D the distance to the star and $\dot{M}$ the mass-loss rate. The intensity measure, I_{scaled}, was then plotted against $\dot{M}/v_{exp}$, where v_{exp} is the expansion velocity. This is used as a proxy for the stellar envelope density. In section 3.2, scatter plots for the identified transitions can be found, each containing I_{scaled} for every source in which this particular transition has been observed.

3

Results and discussion

3.1 Identifications

In Table 3.1, 3.2 and 3.3 all identifications found for the ~ 70 stars from the DEATH-STAR sample studied in this project are listed. Most of the isotopologues searched for (see Table 2.1) were found in the sample. This is not unexpected since the isotopologues have been found in other AGB stars. The ones not found are mostly carbon-rich molecules and less common isotopologues, which are otherwise seen towards only few stars where deep observations have revealed low-intensity lines. However, many of the isotopologues are found in C-type and M-type stars but not in S-type stars (note that all isotopologues were searched for in S-type stars). An explanation for this could be that some isotopologues that are common in C-type stars probably only form if the C/O ratio is high. In a similar way, the isotopologues that are common in M-type stars might only form if the C/O ratio is sufficiently low. The intermediate C/O values of S-type stars mean that one can find some type of mixed chemistry in some cases, but that the prevalence of one or the other set of molecules is not as straightforward. This could also explain why certain isotopologues, for example CS, are found in both C-type and S-type stars while the less common ^{13}CS is only found in C-type stars. Similarly SO is found in both M-type and S-type stars, while the less common ^{34}SO is only found in M-stars.

In Table 3.1, 3.2 and 3.3 some spectral lines have been weighted together to a single line frequency because of their closeness due to fine structure spacing (see Section 2.3). Furthermore, some lines are unidentified, meaning that searching the Splatalogue database did not give any result. In these cases the frequency listed is the middle frequency in the interval searched for in Splatalogue.

Species	Quantum numbers	Frequency [GHz]
COv=0	2-1	230.5380
COv=0	3-2	345.7960
COv=1	3-2	342.6476
^{13}COv=0	3-2	330.5880
SiOv=0	5-4	217.1050
SiOv=1	5-4	215.5960
^{29}SiOv=0	8-7	342.9808
SiSv=0	12-11	217.8177
SiSv=1	12-11	216.7576
SiSv=1	19-18	343.1010
^{29}SiSv=0	13-12	231.6267
^{29}SiSv=1	13-12	230.5098
^{30}SiSv=0	19-18	332.5503
^{30}SiSv=1	19-18	330.9605
Si^{33}Sv=0	13-12	232.6286
CSv=0	7-6	342.8829
^{13}CSv=0	5-4	231.2207
^{13}CN	N=2-1,J=3/2-3/2	217.0735
^{13}CN	N=2-1,J=5/2-3/2	217.2996
^{13}CN	N=2-1,J=5/2-3/2	217.4379
^{13}CN	N=2-1,J=5/2-3/2	217.4682
^{13}CN	N=2-1,J=5/2-1/2	217.6668
C_4Hv=0	N=23-22,J=47/2-45/2,F=24-23	218.8370
C_4Hv=0	N=23-22,J=45/2-43/2,F=23-22	218.8754
C_4Hv=0	N=35-34,J=71/2-69/2,F=36-35	332.9390
C_4Hv=0	N=35-34,J=69/2-67/2,F=35-34	332.9771
C_4Hv_7=1	J=45/2-43/2,Ω=1/2,l=e	218.2875
C_4Hv_7=1	J=45/2-43/2,Ω=1/2,l=f	218.9728
C_4Hv_7=1	J=47/2-45/2,Ω=3/2,l=e	219.0993
C_4Hv_7=1	J=73/2-71/2,Ω=3/2,l=f	343.4431
HC_3Nv=0	J=24-23	218.3247
HC_3Nv=0	J=24-23	218.3248
HC_3Nv=0	J=38-37	345.6090
HC^{15}Nv=0	4-3	344.2001
H^{13}CNv=0	J=4-3	345.3398
H^{13}CNv_2=1	J=4-3,l=1e	345.2387
c-C_3H	4(1,3)-3(1,2),J=7/2-5/2,F=4-3	216.6382
l-C_3Hv=0	J=29/2-27/2,Ω=3/2,F=14-14,l=f	331.0754

Table 3.1: Table listing the name, quantum numbers and frequency for all identifications found for the stars in this sample.

Species	Quantum numbers	Frequency [GHz]
c-HCCCHv=0	3(3,0)-2(2,1)	216.2788
c-HCCCHv=0	16(16,1)-16(15,2)	216.4857
c-HCCCHv=0	5(1,4)-4(2,3)	217.9400
SiN	N=5-4,J=9/2-7/2,F=7/2-7/2	218.0110
SiN	N=5-4,J=11/2-9/2	218.5034
SiC_2v=0	19(2,17)-20(0,20)	218.4413
SiC_2v=0	11(2,10)-11(0,11)	218.7865
SiC_2v=0	10(2,9)-9(2,8)	232.5341
SiC_2v=0	14-13	330.8725
SiC_2v=0	14(2,12)-13(2,11)	346.1100
SiC_2v=0	15(2,14)-14(2,13)	342.8049
SiC_2v=0	15(2,14)-14(2,13)	342.8050
$Si^{13}CC$	10(6,5)-9(6,4)	230.3454
$Si^{13}CC$	10-9	230.9904
$Si^{13}CC$	9(2,7)-8(2,6)	217.1748
$Si^{13}CC$	10(4,7)-9(4,6)	231.7650
$Si^{13}CC$	10(3,8)-9(3,7)	231.8979
$Si^{13}CC$	10(4,6)-9(4,5)	231.9645
$Si^{13}CC$	15(9,6)-14(9,5)	343.4239
AlFv=0	J=7-6,F=15/2-17/2	230.7939
$Na^{37}Cl$v=0	17-16	216.5314
$Na^{37}Cl$v=0	26-25	330.8057
$Na^{37}Cl$v=0	27-26	343.4778
SOv=0	8(8)-7(7)	344.3106
SOv=1	9(8)-8(7)	343.8285
SOv=1	9(8)-8(7)	343.8294
^{33}SO	6-5	217.7877
^{33}SO	9(8)-8(7), F=21/2-19/2	343.0883
^{34}SO	6(5)-5(4)	215.8399
SO_2v=0	22(2,20)-22(1,21)	216.6433
SO_2v=0	85(10,76)-86(7,79)	231.3119
SO_2v=0	26(9,17)-27(8,20)	345.4490
SO_2v=0	11(6,6)-12(5,7)	331.5802
SO_2v=0	21(2,20)-21(1,21)	332.0914
SO_2v=0	4(3,1)-3(2,2)	332.5052
SO_2v=0	37(11,27)-38(10,28)	333.0434
SO_2v=0	29(3,27)-30(0,30)	342.6350
SO_2v=0	34(3,31)-34(2,32)	342.7616

Table 3.2: Same as Table 3.1.

Species	Quantum numbers	Frequency [GHz]
SO_2v_2=1	26(3,23)-26(2,24)	216.7586
SO_2v_2=1	14(3,11)-14(2,12)	231.9805
SO_2v_2=1	6(4,2)-7(3,5)	232.2103
SO_2v_2=1	51(7,45)-52(4,48)	331.9545
SO_2v_2=1	73(8,66)-74(5,69)	331.1092
SO_2v_2=1	24(2,22)-23(3,21)	343.9238
$^{34}SO_2$v=0	55(6,50)-56(3,53)	342.7564
$^{34}SO_2$v=0	29(3,27)-30(0,30)	343.0968
$^{34}SO_2$v=0	10(4,6)-10(3,7)	344.2453
$^{34}SO_2$v=0	23(3,21)-23(2,22)	332.1736
$^{34}SO_2$v=0	16(4,12)-16(3,13)	332.8362
$^{34}SO_2$v=0	17(4,14)-17(3,15)	345.9293
H_2Ov_2=1	5(5,0)-6(4,3)	232.6867
H_2Ov_2=2	3(2,1)-4(1,4)	331.1237
H_2S	2(2,0)-2(1,1)	216.7104
H_2CO	3(0,3)-2(0,2)	218.2222
AlO	N=9-8,J=19/2-17/2,F=10-10	344.4181
AlO	N=9-8,J=19/2-17/2,F=11-11	344.4575
AlO	N=9-8,J=17/2-15/2,F=10-10	344.4675
TiO_2	13(4,10)-12(3,9)	343.2434
unidentified	-	215.5638
unidentified	-	215.5923
unidentified	-	216.2281
unidentified	-	216.4658
unidentified	-	216.6479
unidentified	-	217.7763
unidentified	-	218.5574
unidentified	-	218.5587
unidentified	-	219.1738
unidentified	-	232.2688
unidentified	-	331.0209
unidentified	-	331.0578
unidentified	-	331.0660
unidentified	-	332.8779

Table 3.3: Same as Table 3.1.

3.2 Comparing I_{scaled} with molecular abundance

For all molecular transitions scatter plots were made, where I_{scaled} is plotted against $\dot{M}/v_{exp}$. I_{scaled} and $\dot{M}/v_{exp}$ are treated here as proxies for the molecular abundance and the circumstellar envelope density, respectively. Furthermore, in order to make a comparison with the findings of other papers, some additional plots of the fractional abundance against the density proxy have been included. The molecular transitions discussed here are the ones with enough identifications to make meaningful observations regarding possible trends for the sample. Additionally, I_{scaled} has been calculated for the samples presented in other papers in order to make a more direct comparison with the DEATHSTAR sample. In some cases, a direct comparison between I_{scaled} for the stars in common in the two samples has been made as well. Because there has been no modeling of the molecular abundance in this project, a direct comparison cannot be made. However, it can be discussed whether the intensities in the articles are easily translatable to the abundances and in which way they may correlate or not.

3.2.1 CO

In the DEATHSTAR sample, CO was found in all three chemical types of AGB stars (C-, M- and S-type), see Figure 3.1. In both Figure 3.1a and 3.1b the intensity measure, I_{scaled}, of the CO v=0 line does not seem to depend strongly on the density of the stellar envelope. There is perhaps a slight decrease with increasing density, but it is difficult to say since there are more identifications at lower densities. There is a clear difference in I_{scaled} for C-type and M-type stars, with C-type stars at higher values than M-type stars and S-type stars somewhere in between. This is expected since a higher C/O ratio will mean more carbon available to form CO. In [1] they assume a CO abundance of 2×10^{-4}, 6×10^{-4} and 10^{-3} for M-type, S-type and C-type stars, respectively. This seems to be in line with the relative intensities of the different chemical types in Figure 3.1.

Figure 3.1c shows I_{scaled} for the ^{13}CO J=3-2 line. The distribution does not vary much with density here either although I_{scaled} increases a bit at higher densities, especially for C-type stars. The three different chemical types are a bit more mixed at lower densities but I_{scaled} for C-type stars is generally higher than for M-type stars. The S-type stars, however, have similar or higher I_{scaled} than the C-type stars.

The ^{12}CO J=2-1 and J=3-2 observations are consistent with each other. However, there is a significant difference in I_{scaled} for ^{12}CO and ^{13}CO, about one order of magnitude. This can be explained by the fact that ^{12}CO is much more common than ^{13}CO. For example, [12] finds the ratio of ^{12}CO/^{13}CO to be around 13, 26, and 34 for M-type, S-type and C-type stars respectively for their sample. For an observer, this can often be useful since ^{13}CO emission is not as likely to become optically thick, making it easier to draw reliable conclusions regarding the properties of the observed source.

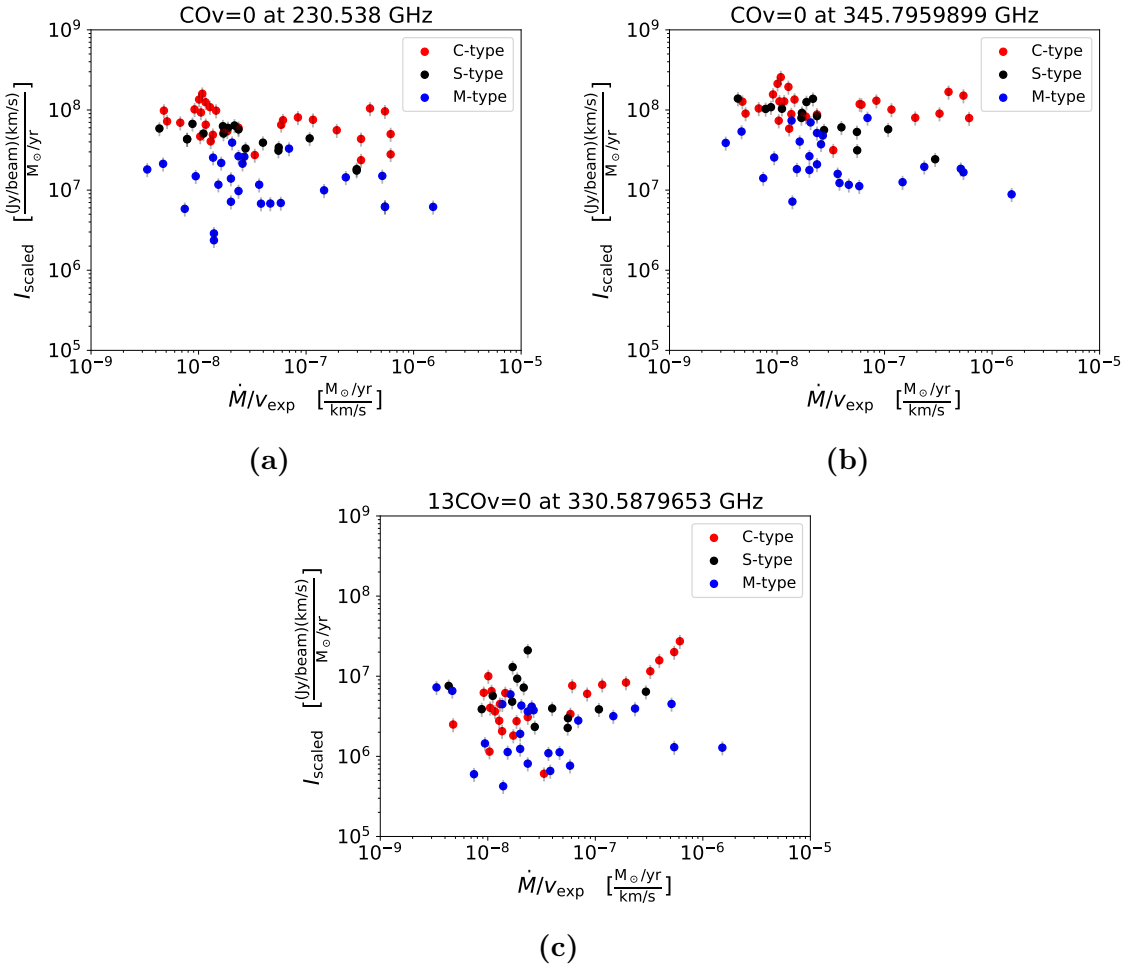

Figure 3.1: Line intensity measure I_{scaled} versus outflow density $\dot{M}/v_{exp}$ for the rotational transitions ^{12}COv=0 J=2-1 (3.1a), ^{12}COv=0 J=3-2 (3.1b) and ^{13}COv=0 J=3-2 (3.1c).

3.2.2 CS, SiS, HCN and SiO

CS, SiS, HCN and SiO are formed in the very inner layers of the CSE and are therefore considered "parent molecules". Somewhat unexpectedly, their abundance does not depend too strongly on the atmospheric C/O [13] and one quite readily detects all four of these molecules towards all chemical types of AGB stars. In Figure 3.2, 3.3, 3.4 and 3.5, I_{scaled} versus $\dot{M}/v_{exp}$ is shown for CS, SiS, HCN (in the form of $H^{13}CN$) and SiO, respectively. In the case of CS, SiS and $H^{13}CN$, I_{scaled} clearly depend on the C/O ratio at the stellar surface (C-type stars having higher I_{scaled} values than S-type and M-type stars). Although this is seen more clearly for CS and $H^{13}CN$. For SiO there does not seem to be as clear of a dependence of I_{scaled} on the C/O ratio. At lower densities M-type stars have higher I_{scaled} values than C-type stars, but at higher densities it is more mixed.

For the CS J=7-6 transition in Figure 3.2a, I_{scaled} for M-type stars seems to increase a bit with stellar envelope density. However, for C-type stars I_{scaled} does not seem to depend strongly on the density. One could perhaps see a trend of I_{scaled} slightly increasing with density but it is difficult to say since there are fewer detections at higher densities. The S-type stars have I_{scaled} values in between the other two chemical types as expected since these stars have a C/O ratio in between the two other chemical types. In Figure 3.2b, ^{13}CS J=5-4 is only detected towards C- and M-type stars in our data. Similarly to Figure 3.2a, the distribution of C-type stars does not seem to vary much with density. For M-type stars there are only a few detections and only at higher densities. Furthermore, I_{scaled} for the ^{13}CS emission is typically one to two orders of magnitude weaker than the corresponding emission from CS. One could claim that this is reasonable since ^{13}CS is far less common than CS (^{12}CO/^{13}CO being around 34 for C-type stars [12] makes ^{12}C much more common than ^{13}C in these stars), but a straight comparison cannot be made since it is not the same transition that is observed.

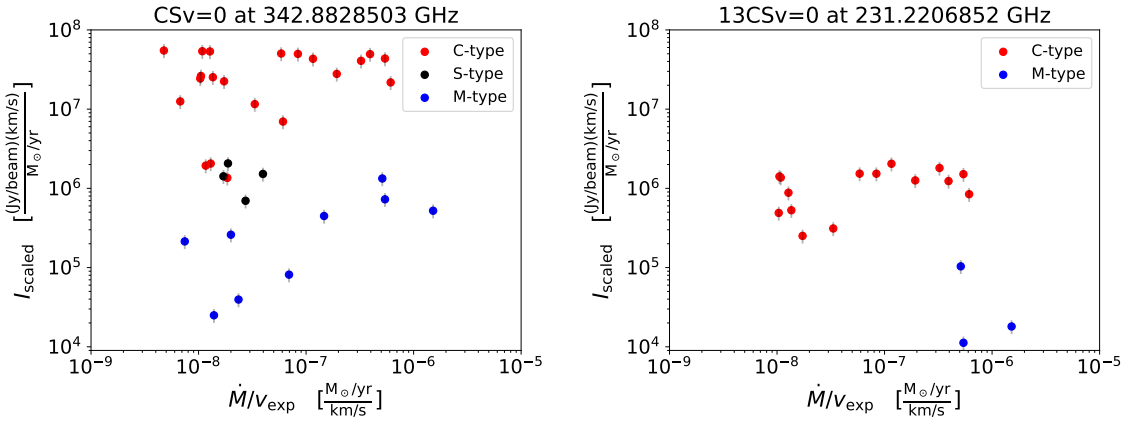

(a) **(b)**

Figure 3.2: Same as Figure 3.1, but for the following rotational transitions: CSv=0 J=7-6 (3.2a) and ^{13}CSv=0 J=5-4 (3.2b).

Figure 3.3 shows several rotational transitions for SiS. There is no clear trend of

I_{scaled} depending strongly on density. Only in Figure 3.3a do we see a slight increase of I_{scaled} with density. Most SiS transitions are only detected towards quite few stars in the sample, making it difficult to draw concrete conclusions regarding potential trends.

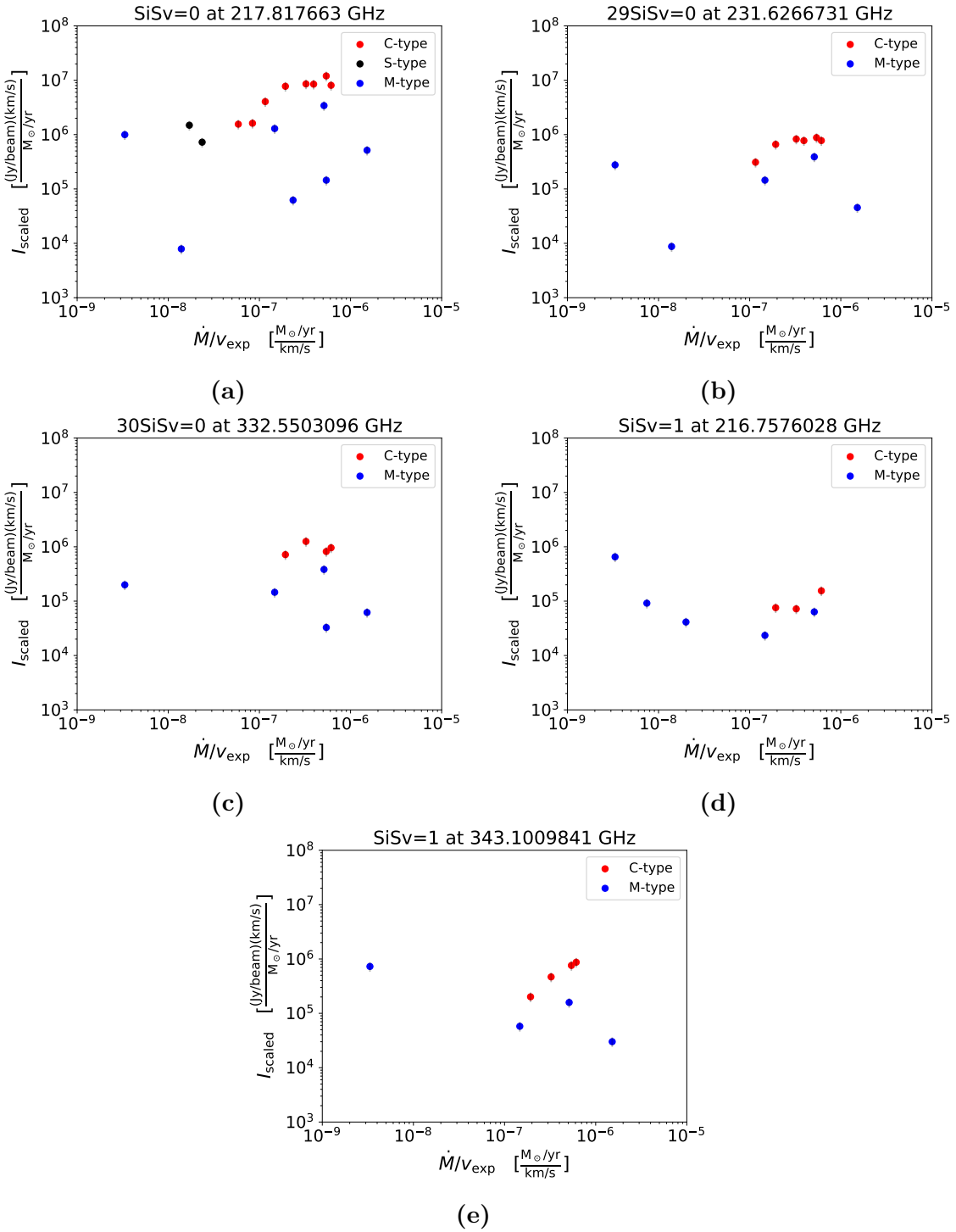

Figure 3.3: Same as Figure 3.1, but for the following rotational transitions: SiSv=0 J=12-11 (3.3a), ^{29}SiSv=0 J=13-12 (3.3b), ^{30}SiSv=0 J=19-18 (3.3c), SiSv=1 J=12-11 (3.3d) and SiSv=1 J=19-18 (3.3e).

For $H^{13}CN$, see Figure 3.4, there is a clear difference in I_{scaled} for the different chemical types of stars, especially at higher densities. Furthermore, I_{scaled} seems to increase with density for C-type stars, while it decreases with density for M-type and S-type stars.

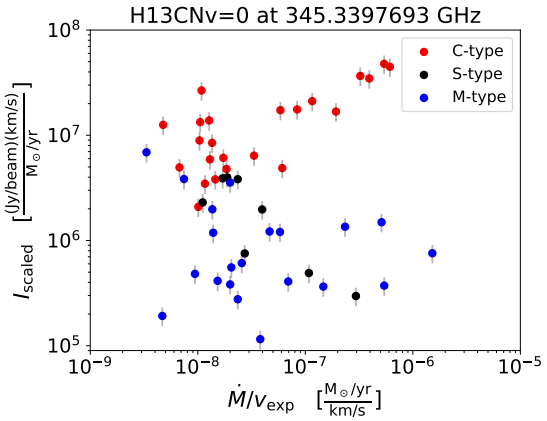

Figure 3.4: Same as Figure 3.1, but for the rotational transition $H^{13}CN$v=0 J=4-3.

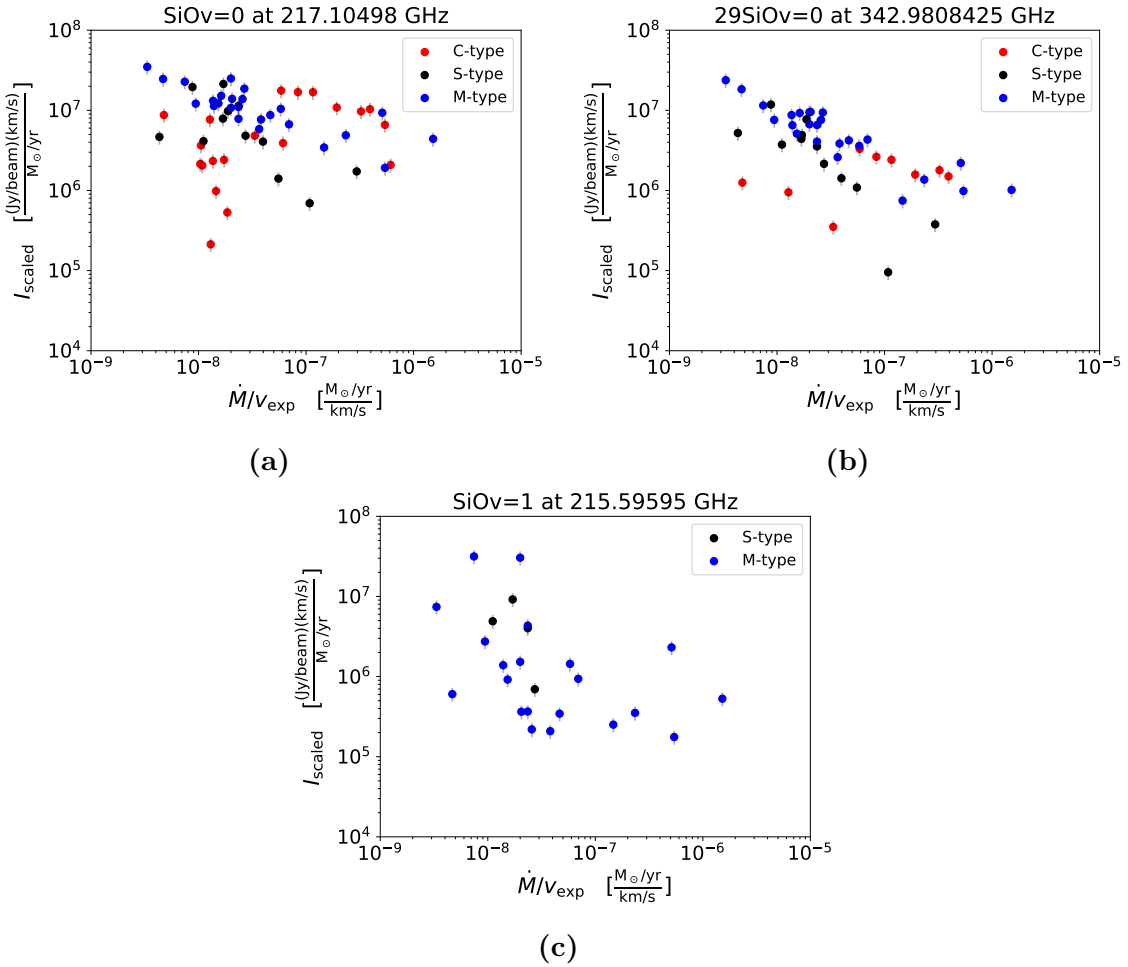

Figure 3.5: Same as Figure 3.1, but for the following rotational transitions: SiOv=0 J=5-4 (3.5a), ^{29}SiOv=0 J=8-7 (3.5b) and SiOv=1 J=5-4 (3.5c) which is a maser line.

In the case of SiO (see Figure 3.5), I_{scaled} for both M-type and S-type stars seems to decrease with density, in contrast to the C-type stars. The decrease in I_{scaled} is seen more clearly in Figure 3.5b compared to Figure 3.5a. Figure 3.5c also shows a trend of decreasing integrated intensity with increasing density. This line, however, is a maser line which makes it more difficult to draw any concrete conclusions from this on the abundance.

In [14] and [15] the fractional abundances of CS, SiS and SiO were modeled. To test how well I_{scaled} can represent the fractional abundance of these molecules, Figures 3.6a, 3.7a and 3.9a were constructed, showing the respective I_{scaled} versus $\dot{M}/v_{exp}$ for the molecular lines used in their abundance modeling. Figures 3.6b, 3.7b and 3.9b show the corresponding modeled fractional abundance of each respective molecule, adopted from the respective papers. The fractional abundance of HCN, modeled in [6], can be seen in Figure 3.8. However, it is not as clear which molecular lines they used in their abundance modeling. Therefore, I_{scaled} has not been calculated for the sample in [6], as it was in the cases of CS, SiS and SiO.

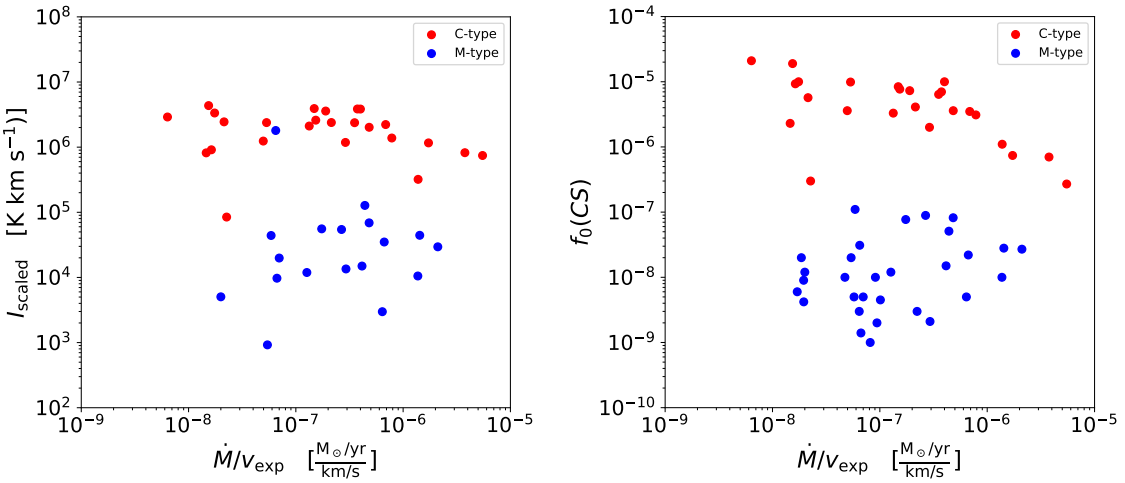

(a) **(b)**

Figure 3.6: I_{scaled} (3.6a) and modeled fractional abundance (3.6b) as a function of $\dot{M}/v_{exp}$ for the full sample in [14] and [15] for the CS rotational transition J=3-2. The red and blue dots represent C-type and M-type stars respectively. The C-type and M-type stars are adopted from [14] and [15], respectively.

In [15] they find that the formation of CS is dependent on the photospheric C/O ratio of the star since there are very clear differences between C- and M-type stars. This seems to be the case for the DEATHSTAR sample as well (see Figure 3.2). CS is detected in all the C-type stars for the sample seen in 3.6b but for the M-type stars it is mostly detected for high mass-loss rates. Furthermore, the modeled CS abundance decreases roughly two orders of magnitude for C-type stars, whereas I_{scaled} for the C-type stars in the DEATHSTAR sample does not vary much with density. I_{scaled} for the M-type stars in the DEATHSTAR sample increases with density while the modeled CS abundances show no clear trend. In [15], the decrease

in CS abundance for the C-type stars leads to them drawing the conclusion that CS is a probable candidate to act as gas-phase precursor of dust grains. In particular of MgS dust grains. This is because collisions between particles and coagulation processes are faster for higher densities. In Figure 3.6a there is not a clear trend of I_{scaled} decreasing with density as there was for the abundance. The distribution looks more similar to that of the DEATHSTAR sample in Figure 3.2.

There is a clear difference between the chemical types in Figure 3.7b, which indicates that the SiS abundance depends on the C/O ratio of the stellar envelope. In [14] they note that in the C-type star envelopes, CS and SiS have abundances of the same order (see Figure 3.6b and 3.7b) and that this probably is a chemical feature related to the envelopes of C-type AGB stars. Furthermore, it is pointed out that SiS is not found in stars with a low mass-loss rate (below 10^{-6} $\dot{M}/yr$) and speculated on whether this could be due to Si and S being trapped in SiO, SiC_2 and CS. The fractional abundance of SiS does not seem to vary with envelope density. A slight decrease in abundance with density can be observed for C-type stars, but much less evidently than for CS. Thus, SiS might be incorporated into dust grains, but not to the same extent [14]. In Figure 3.7a, the distribution of I_{scaled} is similar to that of the DEATHSTAR sample in Figure 3.3. There is a hint of increasing I_{scaled} with increasing density for the C-type stars, but the M-type stars show no clear trend.

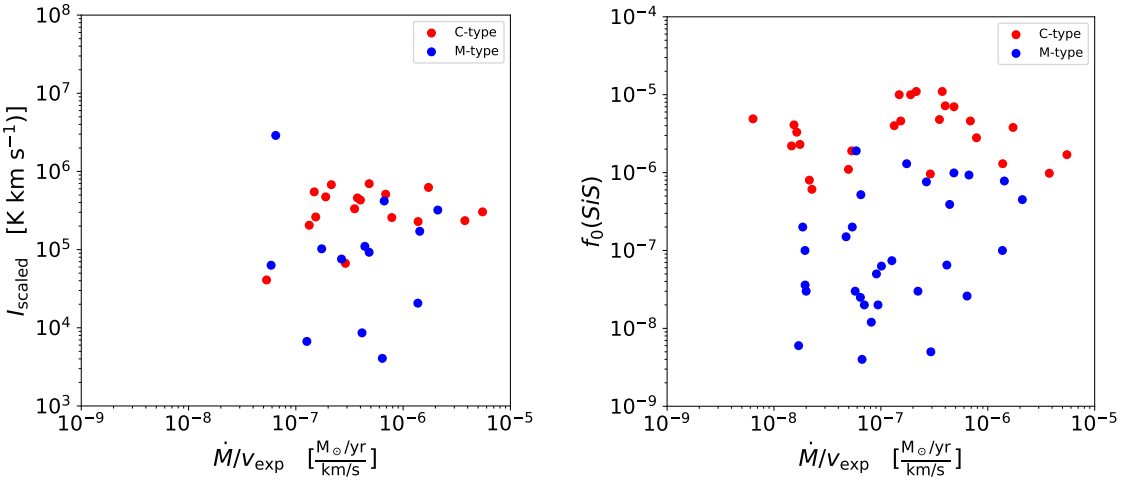

Figure 3.7: Same as for Figure 3.6, but for the SiS rotational transition J=8-7.

The HCN abundance, seen in Figure 3.8, is clearly dependent on the C/O ratio of the circumstellar envelopes. This is the case for I_{scaled} for the DEATHSTAR sample as well (see Figure 3.4). However, note that a comparison between the DEATHSTAR sample and the sample in 3.8 is not straightforward since it is not the same isotopologue being compared. The fractional abundance of the sample from [6] does not seem to vary much with density for any of the chemical types of stars. Since the HCN abundance shows no clear dependence on envelope density, they draw the conclusion in [6] that it is an unlikely gas-phase precursor of dust.

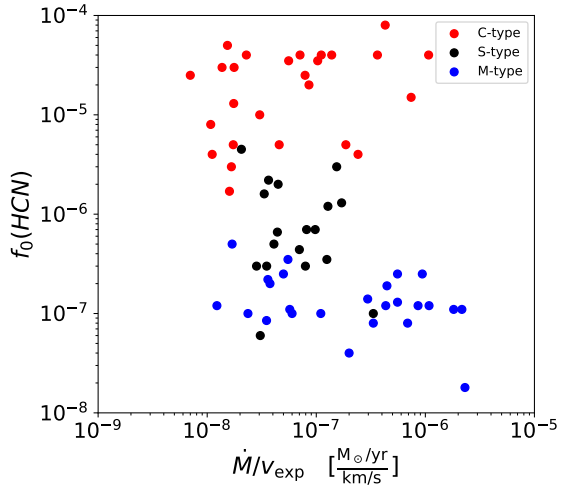

Figure 3.8: Modeled fractional abundance of HCN as a function of $\dot{M}/v_{exp}$ for the sample studied in [6].

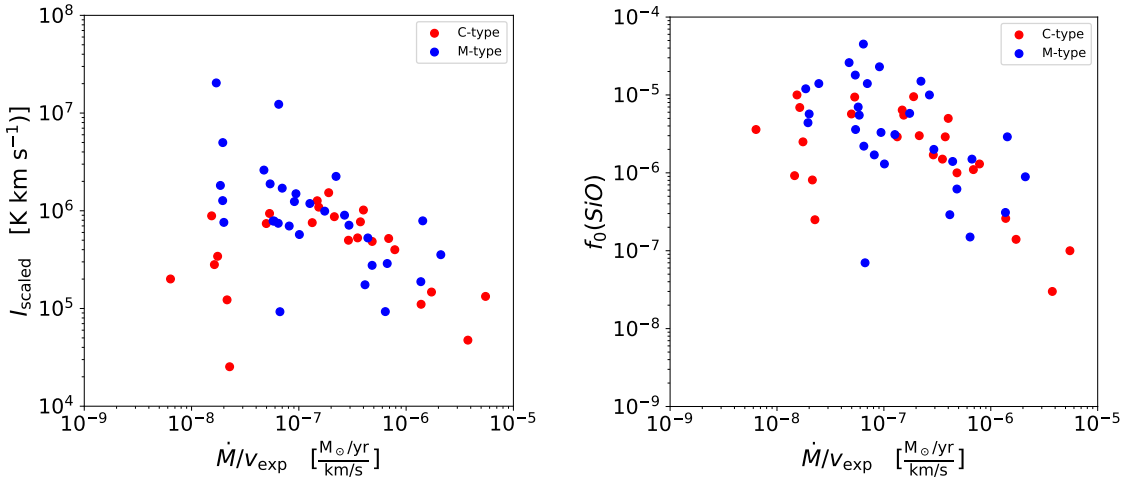

(a) **(b)**

Figure 3.9: Same as for Figure 3.6, but for the SiO rotational transition J=3-2.

The SiO abundance does not seem to depend on the C/O ratio at the stellar surface (see Figure 3.9b), which [15] claims to be in line with theoretical expectations for SiO. The lack of dependence on the C/O ratio can be observed for the DEATHSTAR sample as well (see Figure 3.5). Furthermore, for both C-type and M-type stars they see a clear trend of SiO become less abundant as the envelope density increases. Thus, they draw the conclusion that SiO is a probable candidate to act as a gas-phase precursor of dust grains. In [14] they also note that SiO in general is less abundant than CS and SiS in C-type stars. Figure 3.9a shows similar trends as Figure 3.5 and 3.9b for both C-type and M-type stars, where M-type stars decreases, but C-type stars has "two components", one at low density, and one at high density.

There are a few stars that overlap between the DEATHSTAR sample and the sam-

ples in [14] and [15]. The I_{scaled} values of these stars are shown side by side in Figure 3.10 in order to make a straightforward comparison between the samples. Figure 3.10a shows I_{scaled} calculated from the CS J=3-2 line intensities found in [14] and [15], while 3.10b shows I_{scaled} for the DEATHSTAR sample. Note the difference in unit for I_{scaled} between the two figures and that the mass-loss rates and expansion velocities used in [14] and [15] are slightly different from those used in this project (from [9] and [1]). Therefore, in Figure 3.10 the values found in [14] and [15] were used for the sources from the DEATHSTAR sample as well for this comparison. However, when studying Figure 3.10, it is difficult to draw any clear conclusions, especially since we are comparing two different transitions. The general trend seen for CS in the few stars included here from the DEATHSTAR sample does not contradict the trend seen for the same stars in the sample from [14] and [15], but it does not confirm or strengthen it either. This comparison was done for SiS, SiO and SiC_2 (see section 3.2.3.1) as well, but is not shown here. In all three cases, it was difficult to draw any meaningful conclusions.

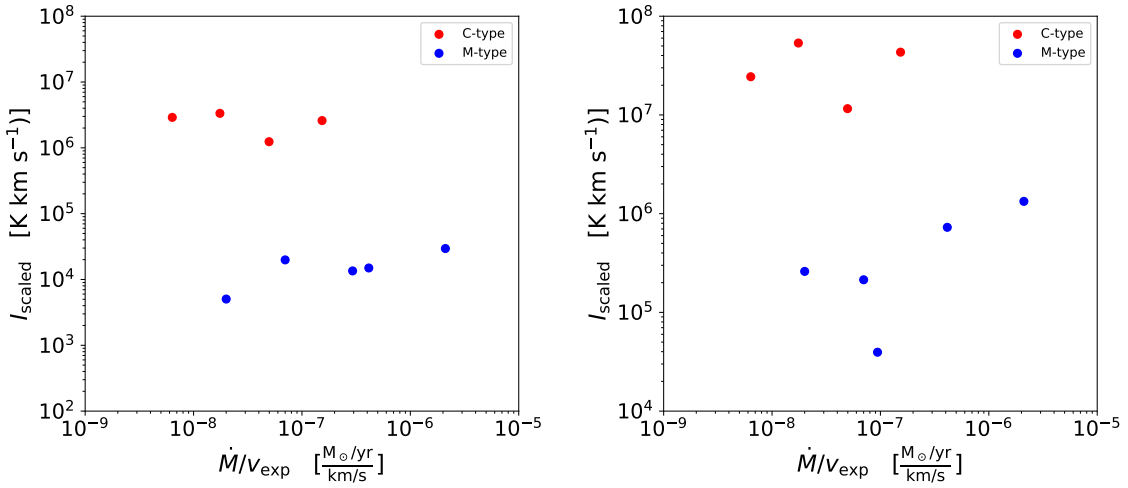

(a) **(b)**

Figure 3.10: Comparison for I_{scaled} between the stars that the sample in [14] and [15] (Figure 3.10a) has in common with the DEATHSTAR sample (Figure 3.10b). The left panel shows I_{scaled} for the CS J=3-2 and the right panel shows I_{scaled} for the CS J=7-6 transition.

3.2.3 Molecules only seen towards C-type stars

3.2.3.1 SiC_2

SiC_2 was searched for in C-type and S-type stars for this sample but was only detected in C-type stars. The lack of detections in S-type stars is likely due to the lower C/O ratio making it more difficult for SiC_2 to form there. Figure 3.11 shows that I_{scaled} does not depend strongly on density.

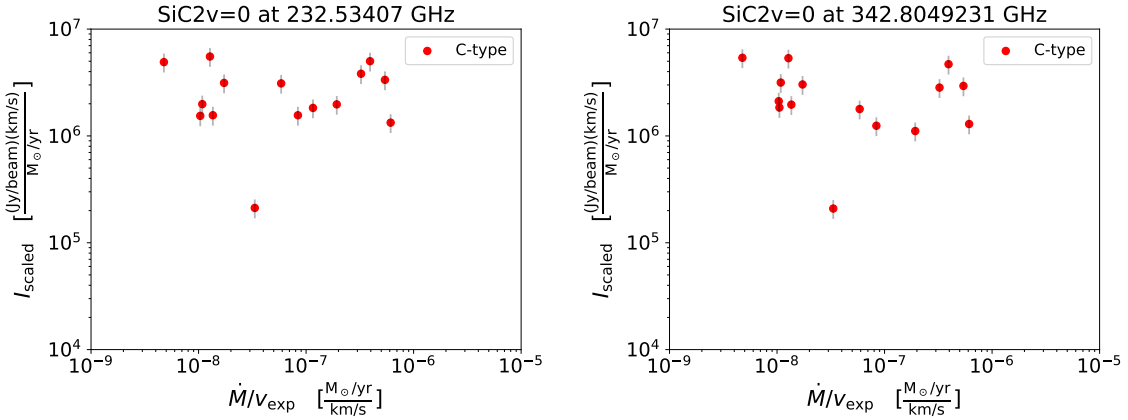

(a) **(b)**

Figure 3.11: Same as Figure 3.1, but for the following rotational transitions: SiC_2v=0 J=10(2,9)-9(2,8) (3.11a) and SiC_2v=0 J=15(2,14)-14(2,13) (3.11b).

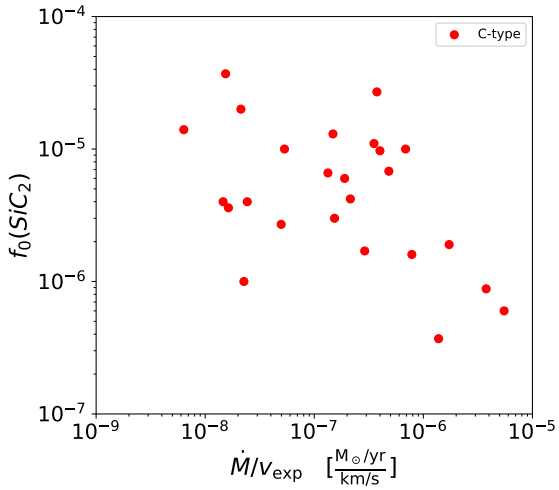

Figure 3.12: Fractional abundance of SiC_2 for the sample studied in [16], where they derive the abundance with the LVG method.

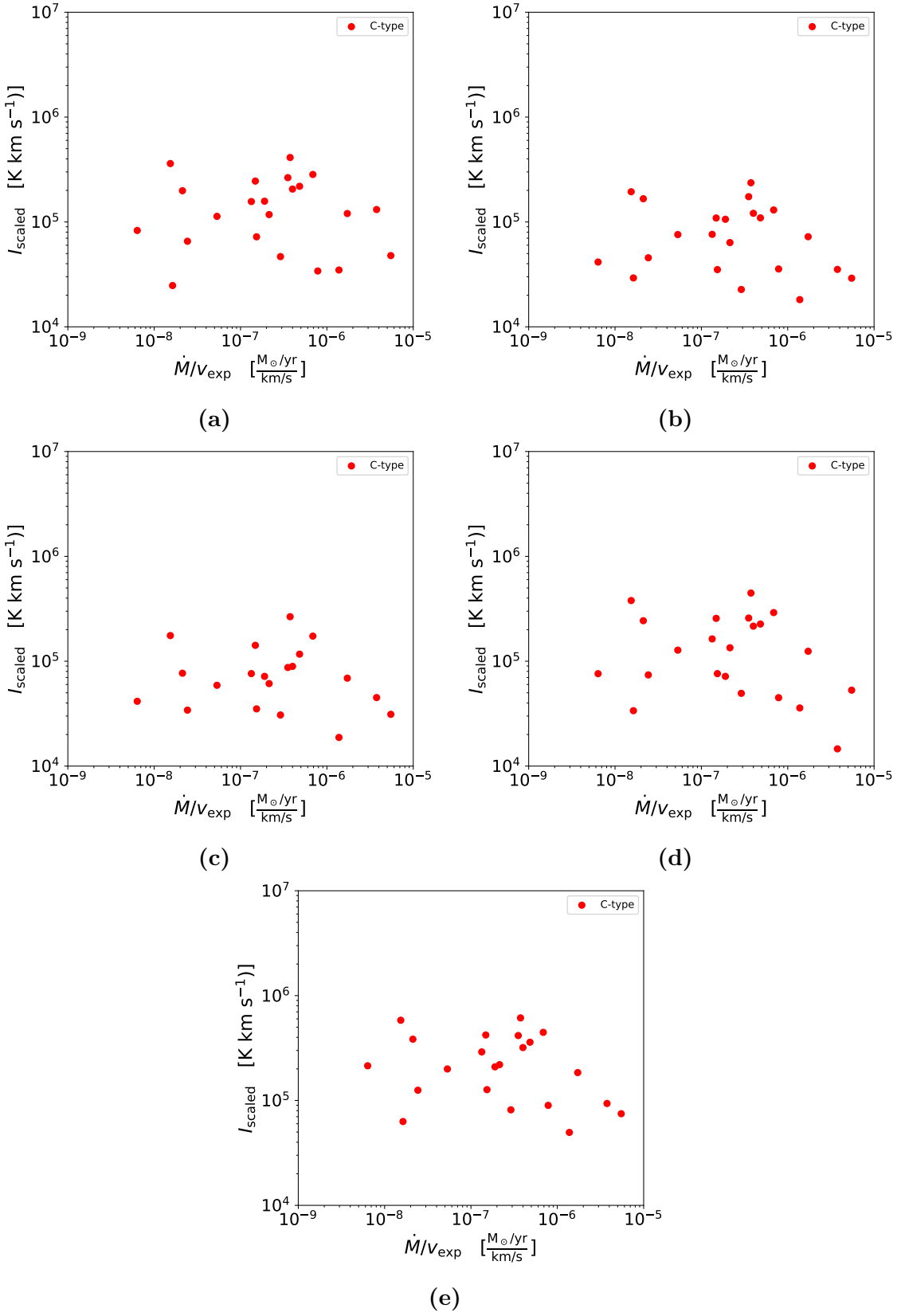

Figure 3.13: I_{scaled} for the sample in [16] for the SiC_2 rotational transitions, J=6(2,5)-5(2,4), J=6(4,3)-5(4,2), J=6(4,2)-5(4,1), J=6(2,4)-5(2,3) and J=7(0,7)-6(0,6), used in their abundance modeling.

A comparison can be made with the result in [16], where a clear trend of decreasing modeled abundance of SiC_2 with envelope density can be observed (see Figure 3.12). In this paper the trend is interpreted as evidence for SiC_2 being incorporated onto dust grains. Their conclusion is that SiC_2 is a likely gas-phase precursor for SiC dust in envelopes around C-type stars, and that it behaves similarly to SiO (see section 3.2.2). The trend seen in Figure 3.12 is not clearly seen for the DEATHSTAR sample when using I_{scaled} as a measure (see Figure 3.11). This could be because the samples are different (only four stars in common), or perhaps because I_{scaled} is only a proxy of the molecular abundance and does not consider radiation transfer. Thus, a straightforward comparison of the two cannot be made. Furthermore, in the case of highly abundant molecules, such as SiC_2, the lines can become optically thick. This means that they are not tracing all the emitting material.

Figure 3.13 shows I_{scaled} for the whole sample in [16], calculated for five different transitions. It is the case for all of them that there is no clear trend of I_{scaled} decreasing with density as there was for the abundance seen in 3.12. The plots look more similar to I_{scaled} for the DEATHSTAR sample seen in Figure 3.11.

3.2.3.2 CN, HC_3N, C_4H and SiN

CN in the form of ^{13}CN, as well as HC_3N, C_4H and SiN was searched for in C-type and S-type stars, but was only detected in C-type stars. In the case of ^{13}CN, as well as HC_3N, C_4H this is reasonable since carbon rich molecules are more likely to be found in stars with a higher C/O ratio.

For ^{13}CN and HC_3N (see Figure 3.14a and 3.14b) there is no clear trend of I_{scaled} decreasing or increasing with density. In the cases of C_4H and SiN there is also no clear trend of I_{scaled} varying much with density (see Figure 3.15 and 3.16). However, one should keep in mind that the number of identifications for C_4H and SiN are very few, making it hard to draw any meaningful conclusions regarding potential trends.

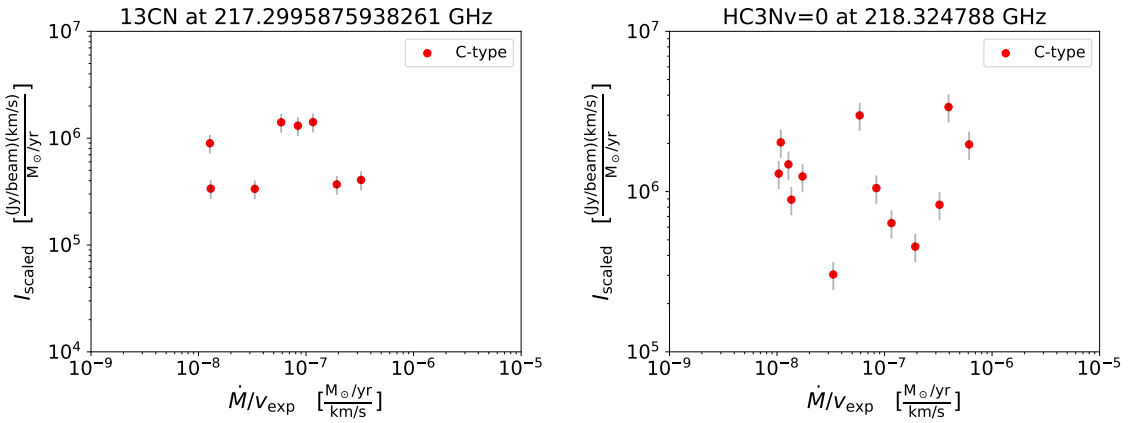

(a) **(b)**

Figure 3.14: Same as Figure 3.1, but for a ^{13}CN spectral line with a weighted transition frequency (3.14a) and the rotational transition HC_3Nv=0 J=24-23 (3.14b).

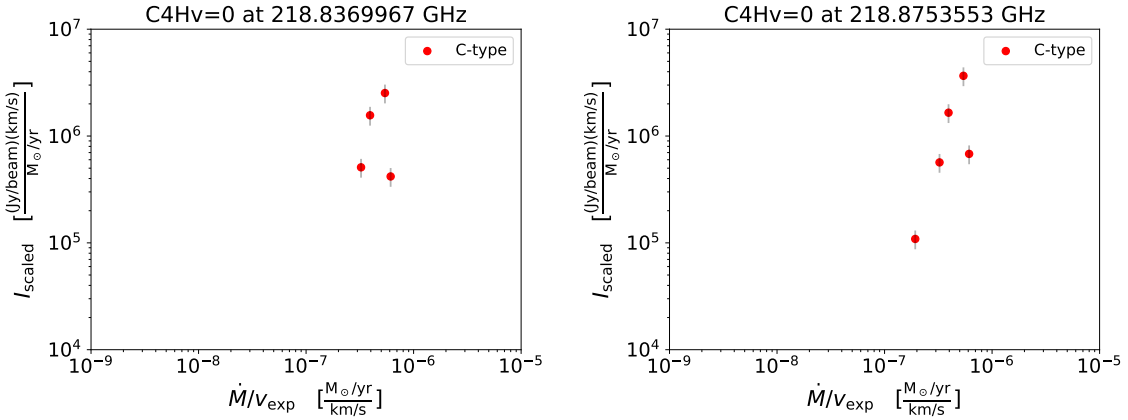

Figure 3.15: Same as Figure 3.1, but for the rotational transitions $C_4Hv=0$ N=23-22,J=47/2-45/2,F=24-23 and $C_4Hv=0$ N=23-22,J=45/2-43/2,F=23-22.

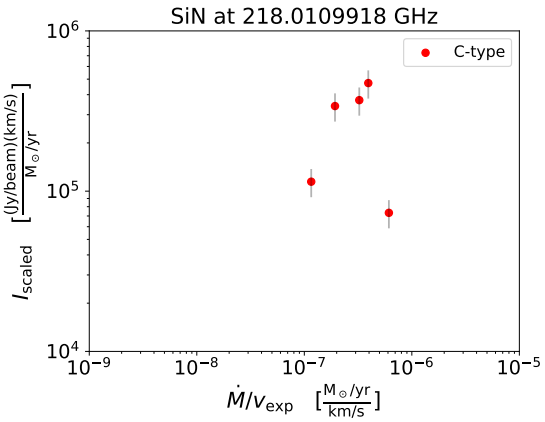

Figure 3.16: Same as Figure 3.1, but for the rotational transition SiN N=5-4,J=9/2-7/2,F=7/2-7/2.

3.2.4 Molecules only seen towards M- and S-type stars

3.2.4.1 SO and SO_2

SO and SO_2 were only detected in M-type and S-type stars in the DEATHSTAR sample. In the case of SO, Figure 3.17 shows that the distribution of I_{scaled} is slightly decreasing with density, but it is clearer for SO (Figure 3.17a) than for ^{34}SO (Figure 3.17b). For SO_2 this trend is also seen (see Figure 3.18), but not as clearly as in the case of for example SiO (see Section 3.2.2).

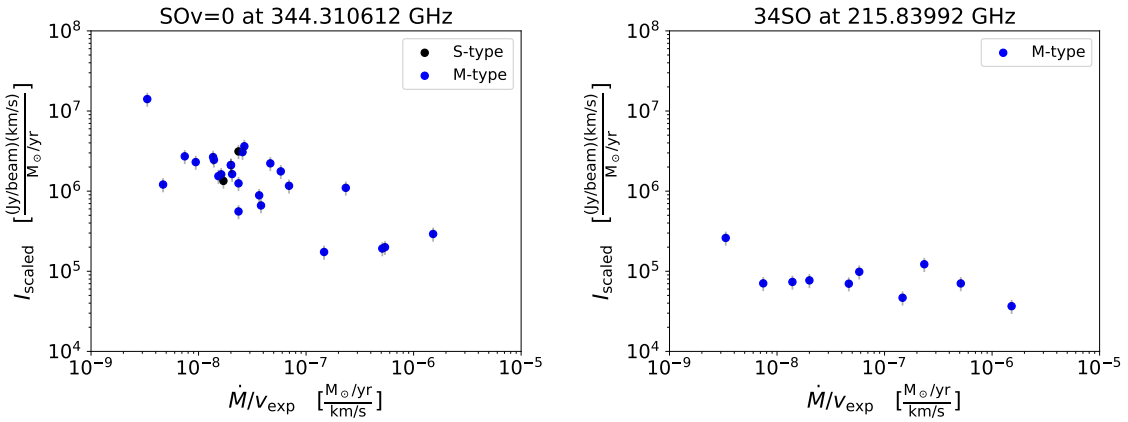

(a) **(b)**

Figure 3.17: Same as Figure 3.1, but for the following rotational transitions: SOv=0 J=8(8)-7(7) (3.17a) and ^{34}SOv=0 J=6(5)-5(4).

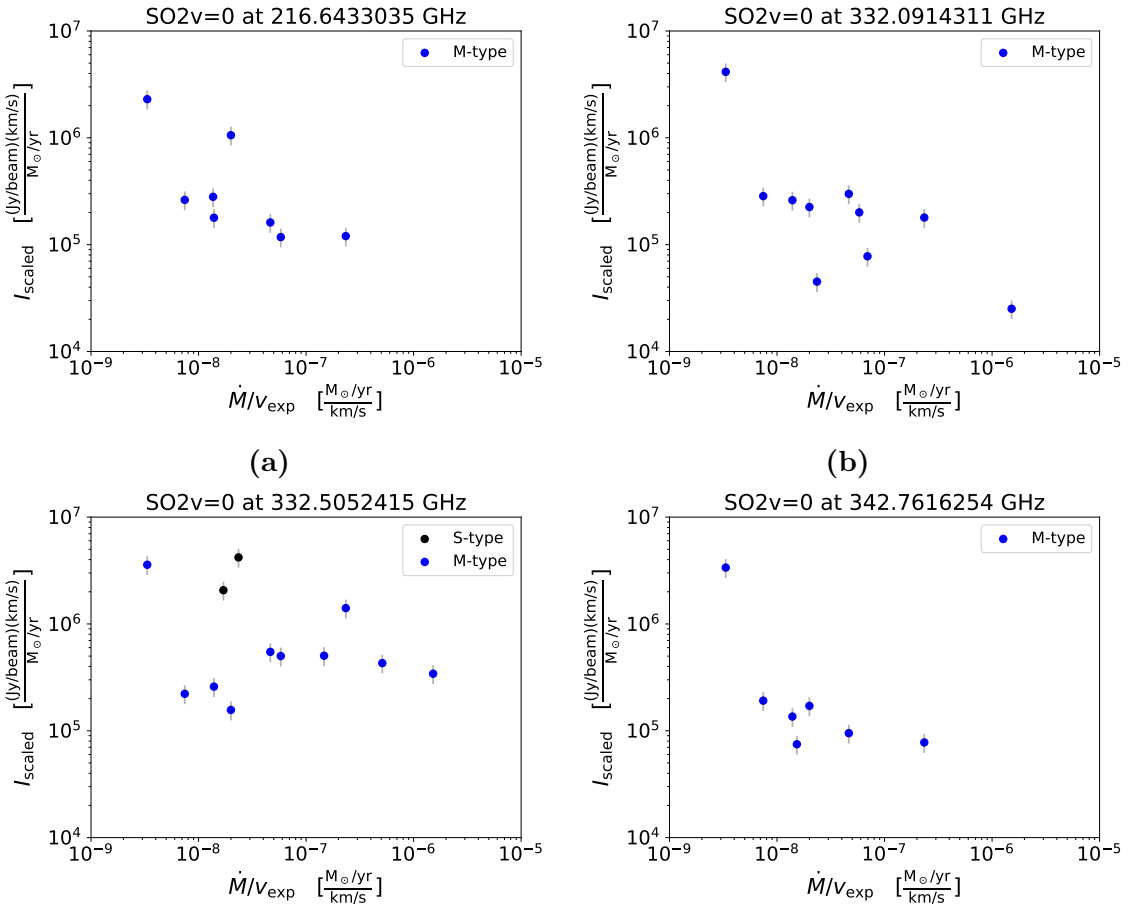

(a) **(b)**

(c) **(d)**

Figure 3.18: Same as Figure 3.1, but for the following rotational transitions: SO_2v=0 J=22(2,20)-22(1,21) (3.18a), SO_2v=0 J=21(2,20)-21(1,21) (3.18b), SO_2v=0 J=4(3,1)-3(2,2) (3.18c) and SO_2v=0 J=34(3,31)-34(2,32) (3.18d).

The sample in [15], seen in Figure 3.19, shows signs of decreasing SO abundance with increasing density (see Figure 3.19b), similarly to I_{scaled} for the DEATHSTAR sample. This leads them to make the conclusion that SO is a possible candidate to act as a gas-phase precursor of dust. However, according to [15], this trend is not as clear as for the case of SiO (see Figure 3.9). In Figure 3.19a, I_{scaled} for the whole sample in [15] is found. There is no clear trend of I_{scaled} decreasing with density, as there was for the DEATHSTAR sample (see in 3.17). One star has a significantly higher I_{scaled} value than the others. This is due to the fact that this star has a much higher measured line intensity (roughly six times higher) than the other stars in the sample. This combined with the star being much further away than most of the stars in the sample leads to a very high estimated I_{scaled} value. Why this star does not stand out as much in Figure 3.19b in the case of modeled abundance is unclear.

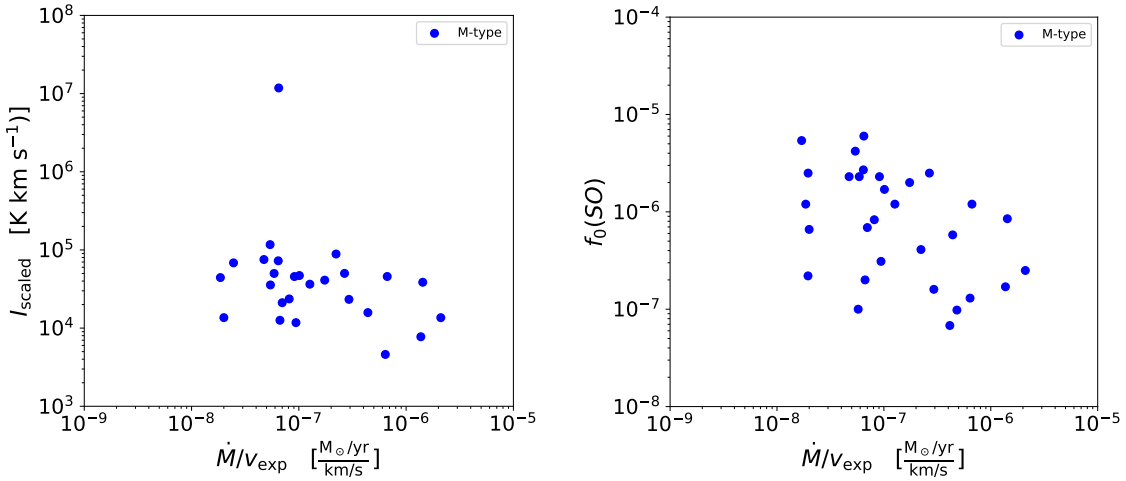

(a) **(b)**

Figure 3.19: Same as for Figure 3.6, but for the SO rotational transition J=3(3)-2(2).

The fractional abundance of SO_2, seen in Figure 3.20, shows no trend of I_{scaled} decreasing with density. Therefore, [15] concludes that SO_2 is an unlikely gas-phase precursor of dust in M-type stellar envelopes. Furthermore, in [15] they note that the abundances of SO and SO_2 are positively correlated, which could mean that there is a chemical connection between the two.

Figure 3.21 shows I_{scaled} for the sample in [15], calculated for the four different transitions they used in their abundance modeling. I_{scaled} shows no trend of decreasing with density, similarly to the fractional abundance seen in Figure 3.20. There is one star with a significantly higher I_{scaled} value here as well. It is the same star as for the case of SO in Figure 3.19a and the explanation is the same in this case as it was for SO.

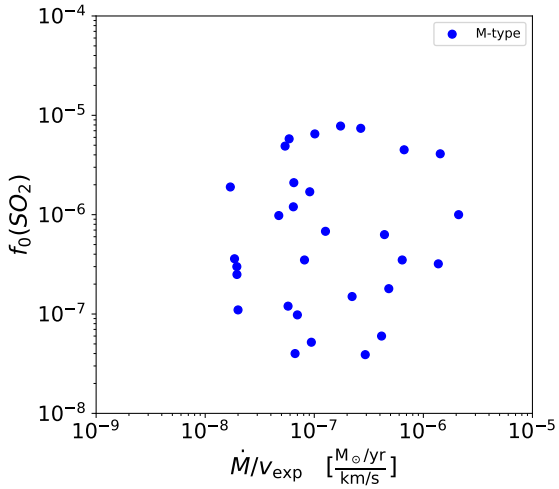

Figure 3.20: Modeled fractional abundance of SO_2 as a function of $\dot{M}/v_{exp}$ for the sample studied in [15].

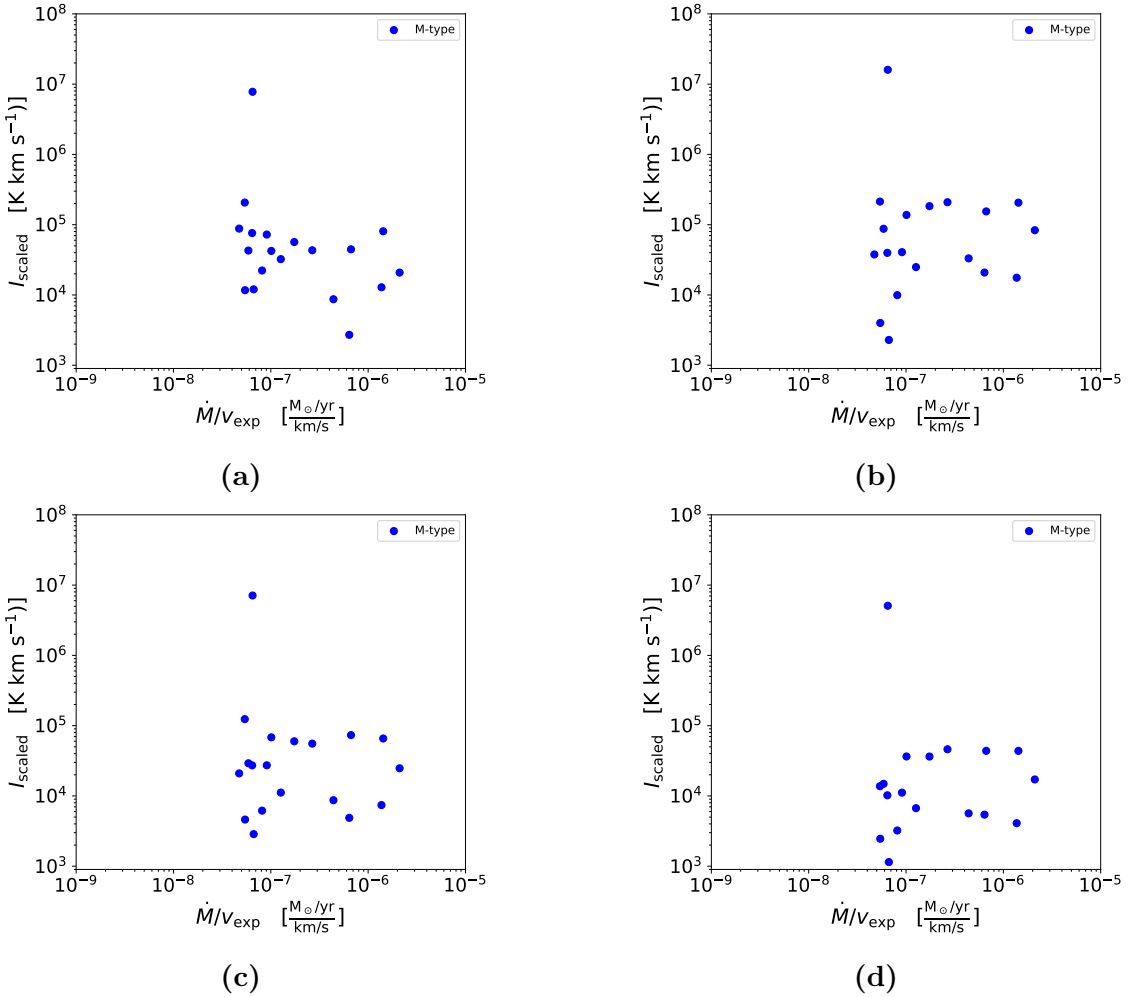

Figure 3.21: Same as for Figure 3.6a, but for the SO_2 rotational transitions: SO_2 J=8(2,6)-8(1,7) (3.21a), SO_2 J=5(1,5)-4(0,4) (3.21b), SO_2 J=4(2,2)-4(1,3) (3.21c) and SO_2 J=2(2,0)-2(1,1) (3.21d).

3.2.4.2 H_2O

H_2O is only detected in M-type stars for this sample. There is a clear trend of I_{scaled} decreasing with density. A possible explanation for the decrease in I_{scaled} could be that water condenses onto the dust particles, since detections of H_2O ice features at infrared wavelengths have been made towards CSEs of M-type stars [17].

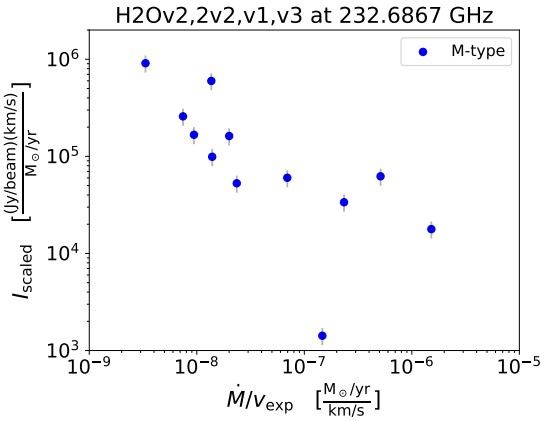

Figure 3.22: Same as Figure 3.1, but for the rotational transition H_2Ov2=1 5(5,0)-6(4,3).

4

Conclusion

In this thesis project ~ 70 AGB stars from the DEATHSTAR project were studied in order to obtain a better understanding of the chemical diversity in the circumstellar envelopes of these stars. This was done by studying features in the eight spectral windows for each source. In order to do this in an efficient way, an automated routine was devised with the purpose of identifying spectral line using the Splatalogue database for astronomical spectroscopy. Most of the isotopologues searched for in the Splatalogue database were found in the sample, which is expected since they have been found in other AGB stars. However, there are still some spectral lines that could not be identified using the Splatalogue database.

For all molecular transitions scatter plots were made, showing I_{scaled} versus $\dot{M}/v_{exp}$, which were treated as proxies for the molecular abundance and the circumstellar envelope density, respectively. In the cases of CS, SiS, HCN, SiO, SiC_2, SO and SO_2 comparisons were made with the fractional abundances modeled in [6], [14], [15] and [16]. No modeling of the molecular abundance was done in this project, which means that a direct comparison with the results in these papers could not be made. Therefore, I_{scaled} was calculated for the molecular lines used in their abundance modeling, in order to make a more direct comparison with the DEATHSTAR sample.

In the case of CS, SiS and $H^{13}CN$, there is a clear dependence of I_{scaled} on the C/O ratio at the stellar surface. This is not the case for SiO. This dependence seems to be translatable to the modeled abundance of the molecules. I_{scaled} for CS and SiS does not seem to depend strongly on density, whereas I_{scaled} for $H^{13}CN$ seems to increase with density for C-type stars, while it decreases with density for M-type and S-type stars. For SiO, I_{scaled} decreases with density for both M-type and S-type stars, while it increases for C-type stars. These trends for I_{scaled} do not translate to the trends seen in the literature for the abundance, except in the case of SiO for which I_{scaled} as well as the abundance seem to decrease with density. There is a decrease in abundance is CS and SiS, while the abundance of HCN does not seem to depend on the density. However, one has to take into account that a direct comparison between HCN and $H^{13}CN$ cannot be made since it is two different isotopologues. For CS and SiS, the calculated I_{scaled} for the molecular lines used in the abundance modeling were not decreasing with density as in the case of the abundance. The trends were more similar to those of CS and SiS in the DEATHSTAR sample. For SiO, this I_{scaled} had a similar trend to both I_{scaled} for the DEATHSTAR sample and

the abundance.

For SiC_2, which was only detected in C-type stars, I_{scaled} does not depend strongly on density, while the modeled abundance of SiC_2 decreases with density. There was no clear trend of I_{scaled} calculated for the molecular lines used in the abundance modeling decreasing with density as there was for the abundance. It is more similar to I_{scaled} for the DEATHSTAR sample. There was no clear trend of decreasing I_{scaled} with density for the other molecules only detected towards C-type stars in the DEATHSTAR sample either.

For SO and SO_2, which were only detected in S- and M-type stars, there was a trend of I_{scaled} slightly decreasing with density. The SO abundance decreases with increasing density, similarly to I_{scaled} for the DEATHSTAR sample. However, this trend is not seen for I_{scaled} calculated for the molecular lines used in the abundance modeling. This could mean that the transition observed by the DEATHSTAR project is a stronger tracer of the abundance. The fractional abundance of SO_2 shows no trend of decreasing with density, which is also the case for I_{scaled} calculated for the corresponding sample. In the case of H_2O, there is a clear trend of I_{scaled} decreasing with density, which could possibly be interpreted as water more efficiently condensing onto the dust particles at higher densities.

In this project we have found that I_{scaled} cannot be easily translated to the abundance. There are some cases, e.g. for SiO, where the trend seen for I_{scaled} is also in seen for the fractional abundance, but in most cases discussed here that is not the case. However, the dependence of I_{scaled} on the C/O ratio at the stellar surface is consistent between I_{scaled} and the abundance. There are currently very few studies that have targeted samples of S-type stars. Thus, the nature of S-type stars is still unclear. In order to better study the chemistry in the stars from this sample, the next step would be to use radiative transfer modeling of the detected molecular lines in order to estimate the molecular abundance.

Bibliography

[1] M. Andriantsaralaza, S. Ramstedt, W. H. T. Vlemmings, T. Danilovich, E. De Beck, M. A. T. Groenewegen, S. Höfner, F. Kerschbaum, T. Khouri, M. Lindqvist, M. Maercker, H. Olofsson, G. Quintana-Lacaci, M. Saberi, R. Sahai, and A. Zijlstra, "DEATHSTAR: nearby AGB stars with the Atacama Compact Array. II. CO envelope sizes and asymmetries: the S-type stars," *Astronomy & Astrophysics*, vol. 653, p. A53, Sep. 2021.

[2] E. De Beck, "Molecular Diagnostics of the Circumstellar Envelopes of Asymptotic Giant Branch Stars. Mass loss and chemistry," Ph.D. dissertation, Katholieke University of Leuven, Astronomical Institute, Jan. 2011.

[3] Hertzsprung-russell diagram. [Online]. Available: https://www.eso.org/public/images/eso0728c/

[4] M. Busso, R. Gallino, and G. J. Wasserburg, "Nucleosynthesis in Asymptotic Giant Branch Stars: Relevance for Galactic Enrichment and Solar System Formation," *Annual Review of Astronomy and Astrophysics*, vol. 37, pp. 239–309, Jan. 1999.

[5] S. Höfner and H. Olofsson, "Mass loss of stars on the asymptotic giant branch. Mechanisms, models and measurements," *The Astronomy and Astrophysics Review*, vol. 26, no. 1, p. 1, Jan. 2018.

[6] F. L. Schöier, S. Ramstedt, H. Olofsson, M. Lindqvist, J. H. Bieging, and K. B. Marvel, "The abundance of HCN in circumstellar envelopes of AGB stars of different chemical type," *Astronomy & Astrophysics*, vol. 550, p. A78, Feb. 2013.

[7] Interstellar and circumstellar medium. [Online]. Available: https://www.asiaa.sinica.edu.tw/research/icsm.php

[8] Masers. [Online]. Available: https://astronomy.swin.edu.au/cosmos/m/Masers

[9] S. Ramstedt, W. H. T. Vlemmings, L. Doan, T. Danilovich, M. Lindqvist, M. Saberi, H. Olofsson, E. De Beck, M. A. T. Groenewegen, S. Höfner, J. H. Kastner, F. Kerschbaum, T. Khouri, M. Maercker, R. Montez, G. Quintana-Lacaci, R. Sahai, D. Tafoya, and A. Zijlstra, "DEATHSTAR: Nearby AGB stars

with the Atacama Compact Array. I. CO envelope sizes and asymmetries: A new hope for accurate mass-loss-rate estimates," *Astronomy & Astrophysics*, vol. 640, p. A133, Aug. 2020.

[10] Splatalogue database for astronomical spectroscopy. [Online]. Available: https://splatalogue.online/

[11] The cologne database for molecular spectroscopy (cdms). [Online]. Available: https://cdms.astro.uni-koeln.de/classic/entries/

[12] S. Ramstedt and H. Olofsson, "The $^{12}CO/^{13}CO$ ratio in AGB stars of different chemical type. Connection to the $^{12}C/^{13}C$ ratio and the evolution along the AGB," *Astronomy & Astrophysics*, vol. 566, p. A145, Jun. 2014.

[13] L. Decin, I. Cherchneff, S. Hony, S. Dehaes, C. De Breuck, and K. M. Menten, "Detection of "parent" molecules from the inner wind of AGB stars as tracers of non-equilibrium chemistry," *Astronomy & Astrophysics*, vol. 480, no. 2, pp. 431–438, Mar. 2008.

[14] S. Massalkhi, M. Agúndez, and J. Cernicharo, "Study of CS, SiO, and SiS abundances in carbon star envelopes: assessing their role as gas-phase precursors of dust," *Astronomy & Astrophysics*, vol. 628, p. A62, Aug. 2019.

[15] S. Massalkhi, M. Agúndez, J. Cernicharo, and L. Velilla-Prieto, "The abundance of S- and Si-bearing molecules in O-rich circumstellar envelopes of AGB stars," *Astronomy & Astrophysics*, vol. 641, p. A57, Sep. 2020.

[16] S. Massalkhi, M. Agúndez, J. Cernicharo, L. Velilla Prieto, J. R. Goicoechea, G. Quintana-Lacaci, J. P. Fonfría, J. Alcolea, and V. Bujarrabal, "Abundance of SiC_2 in carbon star envelopes," *Astronomy & Astrophysics*, vol. 611, p. A29, Mar. 2018.

[17] F. J. Molster, L. B. F. M. Waters, and F. Kemper, "The Mineralogy of Interstellar and Circumstellar Dust in Galaxies," in *Lecture Notes in Physics, Berlin Springer Verlag*, T. Henning, Ed., 2010, vol. 815, pp. 143–201.

DEPARTMENT OF PHYSICS
CHALMERS UNIVERSITY OF TECHNOLOGY
Gothenburg, Sweden
www.chalmers.se

CHALMERS
UNIVERSITY OF TECHNOLOGY